SLAC-PUB-10824
astro-ph/0410319
October 2004

Microlensing Optical Depth towards the Galactic Bulge Using Clump Giants from the MACHO Survey

P. Popowski[1], K. Griest[2], C.L. Thomas[2], K.H. Cook[3], D.P. Bennett[4], A.C. Becker[5], D.R. Alves[6], D. Minniti[7], A.J. Drake[7], C. Alcock[8], R.A. Allsman[9], T.S. Axelrod[10], K.C. Freeman[11], M. Geha[12], M.J. Lehner[13], S.L. Marshall[14], C.A. Nelson[3], B.A. Peterson[11], P.J. Quinn[15], C.W. Stubbs[8], W. Sutherland[16], T. Vandehei[2], D. Welch[17]
(The MACHO Collaboration)

ABSTRACT

Using 7 years of MACHO survey data, we present a new determination of the optical depth to microlensing towards the Galactic bulge. We select the sample of 62 microlensing events (60 unique) on clump giant sources and perform a detailed efficiency analysis. We use only the clump giant sources because these are bright bulge stars and are not as strongly affected by blending. Using a subsample of 42 clump events concentrated in just 4.5 deg^2, we find $\tau = 2.17^{+0.47}_{-0.38} \times 10^{-6}$ at $(l, b) = (1.^\circ 50, -2.^\circ 68)$, somewhat smaller than found in most previous MACHO studies, but in excellent agreement with recent theoretical predictions. We also present the optical depth in each of the 19 fields in which we detected events, and find limits on optical depth for fields with no events. The errors in optical depth in individual fields are dominated by Poisson noise. We measure optical depth gradients of $(1.06 \pm 0.71) \times 10^{-6}\mathrm{deg}^{-1}$ and $(0.29 \pm 0.43) \times 10^{-6}\mathrm{deg}^{-1}$ in the galactic latitude b and longitude l directions, respectively. Finally, we discuss the possibility of anomalous duration distribution of events in the field 104 centered on $(l, b) = (3.^\circ 11, -3.^\circ 01)$ as well as investigate spatial clustering of events in all fields.

Subject headings: Galaxy: center, stellar content, structure — gravitational lensing — surveys

[1]Max-Planck-Institute for Astrophysics, Karl-Schwarzschild-Str. 1, Postfach 1317, 85741 Garching bei München, Germany
Email: popowski@mpa-garching.mpg.de

[2]Department of Physics, University of California, San Diego, CA 92093, USA
Email: griest@astrophys.ucsd.edu, clt@ucsd.edu, vandehei@astrophys.ucsd.edu

[3]Lawrence Livermore National Laboratory, Livermore, CA 94550, USA
Email: kcook, cnelson@igpp.ucllnl.org

[4]Department of Physics, University of Notre Dame, IN 46556, USA
Email: bennett@emu.phys.nd.edu

[5]Astronomy Department, University of Washington, Seattle, WA 98195, USA
Email: becker@astro.washington.edu

[6]Laboratory for Astronomy & Solar Physics, Goddard Space Flight Center, Code 680, Greenbelt, MD 20781, USA
Email: alves@lasp680.gsfc.nasa.gov

[7]Departmento de Astronomia, Pontifica Universidad Catolica, Casilla 104, Santiago 22, Chile
Email: dante, ajd@astro.puc.cl

[8]Harvard-Smithsonian Center for Astrophysics, 60 Garden St., Cambridge, MA 02138, USA
Email: calcock, cstubbs@cfa.harvard.edu

[9]NOAO, 950 North Cherry Ave., Tucson, AZ 85719, USA
Email: robyn@noao.edu

[10]Steward Observatory, University of Arizona, Tucson, AZ 85721, USA
Email: taxelrod@as.arizona.edu

[11]Research School of Astronomy and Astrophysics, Canberra, Weston Creek, ACT 2611, Australia
Email: kcf, peterson@mso.anu.edu.au

[12]Carnegie Observatories, 813 Santa Barbara Street, Pasadena, CA 91101, USA
Email: mgeha@ociw.edu

[13]Department of Physics and Astronomy, University of Pennsylvania, PA 19104, USA
Email: mlehner@hep.upenn.edu

[14]SLAC/KIPAC, 2575 Sand Hill Rd., MS 29, Menlo Park, CA 94025, USA
Email: marshall@slac.stanford.edu

[15]European Southern Observatory, Karl-Schwarzschild-Str. 2, 85748 Garching bei München, Germany
Email: pjq@eso.org

[16]Institute of Astronomy, University of Cambridge, Madingley

Work supported in part by the Department of Energy Contract DE-AC02-76SF00515
Stanford Linear Accelerator Center, Stanford University, Stanford, CA 94309

1. Introduction

The structure and composition of our Galaxy is one of the outstanding problems in contemporary astrophysics. Microlensing is a powerful tool to learn about massive objects in the Galaxy. The amount of matter between the source and observer is typically described in terms of the microlensing optical depth, which is defined as the probability that a source flux will be gravitationally magnified by more than a factor of 1.34. Early predictions (Griest et al. 1991; Paczyński 1991) of the optical depth towards the Galactic center included only disk lenses and found values near $\tau = 0.5 \times 10^{-6}$. The early detection rate (Udalski et al. 1993, 1994a) seemed higher, and further calculations (Kiraga & Paczyński 1994) added bulge stars to bring the prediction up to 0.85×10^{-6}. The first measurements were substantially higher than this: $\tau \geq 3.3 \pm 1.2 \times 10^{-6}$ at the location of Baade's Window (Udalski et al. 1994b) based upon 9 events and $\tau = 3.9^{+1.8}_{-1.2} \times 10^{-6}$ at $(l, b) = (2.^{\circ}52, -3.^{\circ}64)$ (Alcock et al. 1997a) based upon 13 clump-giant events and an efficiency calculation. Many additional theoretical studies ensued, including additional effects, especially non-axisymmetric components such as a bar (e.g., Zhao, Spergel & Rich 1995; Metcalf 1995; Zhao & Mao 1996; Bissantz et al. 1997; Gyuk 1999; Nair & Miralda-Escudé 1999; Binney, Bissantz & Gerhard 2000; Sevenster & Kalnajs 2001; Evans & Belokurov 2002; Han & Gould 2003). Values in the range 0.8×10^{-6} to 2×10^{-6} were predicted for various models, and values as large 4×10^{-6} were found to be inconsistent with almost any model.

More recent measurements using efficiency calculations found values of $\tau = 3.23^{+0.52}_{-0.50} \times 10^{-6}$ at $(l, b) = (2.^{\circ}68, -3.^{\circ}35)$ from 99 events in 8 fields using difference image analysis (Alcock et al. 2000a), $\tau = 3.36^{+1.11}_{-0.81} \times 10^{-6}$ at $(l, b) \approx (1.^{\circ}0, -3.^{\circ}9)$ from 28 events using difference image analysis[18] (Sumi et al. 2003), $\tau = 2.0 \pm 0.4 \times 10^{-6}$ at $(l, b) = (3.^{\circ}9, -3.^{\circ}8)$ from around 50 clump-giant events in a preliminary version of this paper (Popowski et al. 2001a), and $\tau = 0.94 \pm 0.29 \times 10^{-6}$ at $(l, b) = (2.^{\circ}5, -4.^{\circ}0)$ from 16 clump-giant events (Afonso et al. 2003).

Blending is a major problem in any analysis of the microlensing data involving point spread function photometry. The bulge fields are crowded, so that the objects observed at a certain atmospheric seeing are blends of several stars. At the same time, typically only one star is lensed. In this general case, a determination of the events' parameters and the analysis of the detection efficiency of microlensing events is very involved and vulnerable to a number of possible systematic errors. If the sources are bright, one can avoid these problems. First, a determination of parameters of the actual microlensing events becomes straightforward. Second, it is sufficient to estimate detection efficiency based on the sampling of the light curve alone. This eliminates the need of obtaining deep luminosity functions across the bulge fields. Red clump giants are among the brightest and most numerous stars in the bulge, so we focus on these stars here. An optical depth determination using all observed microlensing events would be desirable, but would require an accurate calculation of the blending efficiency for non-clump stars, demanding much additional input including HST quality images and luminosity functions over much of the bulge.

The structure of this paper is the following. In § 2 we briefly describe the MACHO experiment as the source of the data used here. Section 3 is devoted to the selection of microlensing events. In particular, we discuss how we select our sample of 62 clump giant events (60 unique) and its relation to the catalog of over 500 events constructed by Thomas et al. (2004, companion paper). In § 4 we test our sample for signatures of blending. Optical depth toward the Galactic bulge is derived in § 5. In § 6 we consider spatial distribution of events and discuss the significance of some apparent clusters seen in the data. We summarize our results in § 7.

Road, Cambridge. CB3 0HA, U.K.
Email: wjs@ast.cam.ac.uk

[17]McMaster University, Hamilton, Ontario Canada L8S 4M1
Email: welch@physics.mcmaster.ca

[18]We would like to notice here that the results from the difference image analyses cannot be easily compared to the ones from clump analyses. The analyses that use clump giant sources have reasonably good control over the location of sources they are sensitive to: the bulge clump giants dominate over any other possible locations. Difference image determinations are sensitive to all sources along the line of sight, and thus the determined optical depth is characteristic for the direction only and cannot be claimed to be the optical depth toward the bulge. A typically employed remedy is to assume that the only two populations of sources that matter in star counts are: the bulge one and the foreground disk one, and that only bulge sources contribute to the optical depth. Following on this assumption, one corrects a measured optical depth by a fudge factor that is supposed to account for the number of inefficient disk sources. It is not clear whether such correction is needed and the size of it is very uncertain. The results we quote include this correction. The optical depth values without these controversial corrections are about 20% lower for both MACHO and MOA.

2. Data

The MACHO Project had full-time use of the 1.27 meter telescope at Mount Stromlo Observatory, Australia from July 1992 until December 1999. Details of the telescope system are given by Hart et al. (1996), and details of the camera system by Stubbs et al. (1993) and Marshall et al. (1994). Briefly, corrective optics and a dichroic were used to give simultaneous imaging of a 43'$\times$ 43' fields in two bands, using eight 2048^2 pixel CCD's. A total of 32700 exposures were taken in 94 fields (Figure 1) towards the Milky Way bulge resulting in around 3 Tbytes of raw image data and light curves on 50.2 million stars. The coverage of fields varies greatly from 12 observations of field 106 to 1815 observations of field 119. Note that the observing strategy changed several times during the project, so even in a given field the frequency of observations changes from year to year. In addition, the bulge was not observed at all during the prime LMC observing times, so all bulge lightcurves have gaps during November-February.

In this paper, we analyze 7 seasons of Galactic bulge data. We select a subsample of 62 clump-giant events (60 unique events and 2 duplicate events) from 337 selection criteria C events listed in our catalog of more than 500 bulge microlensing events constructed by Thomas et al. (2004, companion paper). For the optical depth determination, we exclude eleven fields in 300 series. The excluded fields are close to the Galactic plane but are relatively distant from the Galactic center. As a result, they are dominated by the disk stars, which complicates the morphology of the color-magnitude diagram and renders the selection of clump giants much more difficult.

For photometric calibrations, we used global, chunk uncorrected relations that express Johnson's V and Kron-Cousins' R in terms of the MACHO intrinsic magnitudes b_M and r_M as:

$$V = b_M - 0.18(b_M - r_M) + 23.70, \qquad (1)$$

$$R = r_M + 0.18(b_M - r_M) + 23.41. \qquad (2)$$

For more details see Alcock et al. (1999).

3. Selection of Events for Optical Depth Determination

3.1. Event Selection

The microlensing events are selected based on several levels of cuts using statistics calculated for the

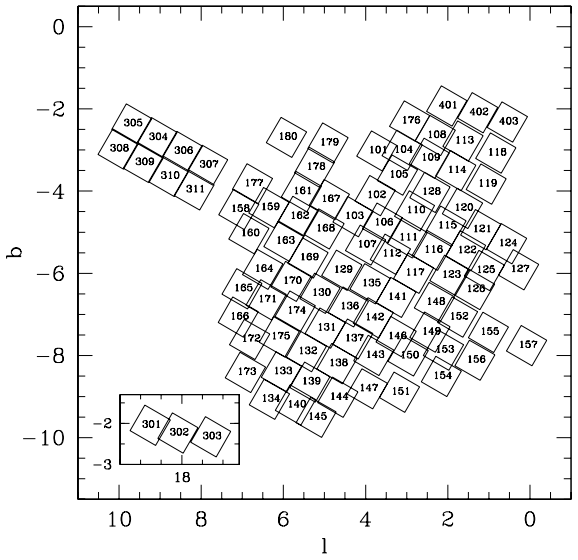

Fig. 1.— Location of all 94 MACHO fields [including 3 high-longitude fields at $(l, b) \sim (18, -2)$]. The clump regions in fields 300 through 311 are expected to be contaminated by disk stars, and thus these fields are not included in the optical depth determination.

lightcurves. We denote as level-0, all 50.2 million lightcurves in our database. Using a small set of variability and "bump-finding" statistics, a few percent of the lightcurves are advanced to level-1. The complete set of over 150 statistics, including non-linear fits to microlensing lightcurve shape, is calculated for all these lightcurves and around 90000 are advanced to level 1.5. Final selection (level-2) is made after fine tuning the selection criteria to maximize inclusion of genuine microlensing events and minimize inclusion of variable stars, supernovae, noise, etc. A more thorough description of the most useful statistics is given in Alcock et al. (2000b). Table 1 gives a brief summary of the selection criteria used here, many of which measure signal/noise and goodness-of-fit to a microlensing lightcurve shape.

To differentiate the current set of level-2 cuts from the cuts used previously and from the cuts used to select LMC microlensing events, we denote the current set of cuts as "selection criteria C". It is crucial to use exactly this set of selection criteria on the artificial microlensing events we create to calculate our detection efficiency.

A total of 337 stars passed selection criteria C, 62

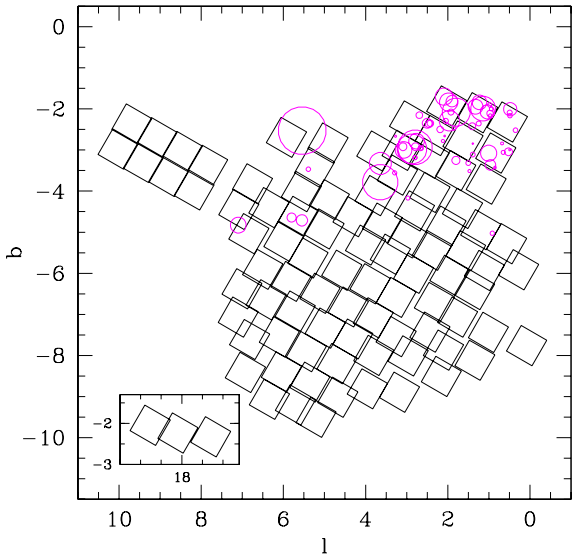

Fig. 2.— Spatial distribution of events with clump giants as sources. Radii of circles are scaled as $t/\epsilon(t, A_{max})$ (See appendix A). The clump region in fields 300 through 311 (Fig. 1) are expected to be contaminated by disk stars, and thus clump giant events are not selected in those fields.

of which are clump giants (a total of 531 events are reported in the companion paper, 450 of which were denoted high quality; these were found with a less restrictive selection). Figure 2 shows the position of the clump events on the sky. Clump giant stars are found by final additional cuts on the color-magnitude diagram (CMD). This selection differs from the selection used in Alcock et al. (1997a). A detailed description of the clump giant selection is given in the next subsection. The full lightcurves of the microlensing events are shown in the companion paper (Thomas et al. 2004).

3.2. Clump Giant Selection

Selection of bulge clump giant sources is important since any non-giant or non-bulge source stars mistakenly included will distort the optical depth result due to being heavily blended or being at the wrong distance. While clump giants form a well defined population the very patchy extinction towards the Galactic center makes selection more complicated. We have attempted to correct for this effect in a more sophisticated way than in the past, but the possibility for contamination still exists.

The question, which of our sources may be clump giants, is first investigated through the analysis of the global properties of the color-magnitude diagram in the Galactic bulge. Using the accurately measured extinction towards Baade's Window (Stanek 1996 with zero point correction according to Gould, Popowski, & Terndrup 1998 and Alcock et al. 1998) allows us to locate *bulge* clump giants on the dereddened color-magnitude diagram. Such diagram can be then used to predict the positions of clump giants on the color-apparent magnitude diagram for fields with different extinction. Based on Baade's Window data we conclude that unreddened clump giants are present in the color range $(V-R)_0 \in (0.40, 0.60)$, and they concentrate along a line $V_0 = 14.35 + 2.0\,(V-R)_0$, where the zero point of this line is likely uncertain at the level of at least 0.1 mags[19]. We assume that the actual clump giants scatter in V_0 magnitude around these central values, but by not more than 0.6-0.7 mag toward both fainter and brighter V_0. This range of magnitudes is designed to include both the population scatter and the distance dispersion of clump giants along the line of sight. The parallelogram-shaped box in the upper left corner of Figure 3 is approximately defined by the above assumptions. To be exact, we define this parallelogram to have the following vertex points in $[(V-R)_0, V_0]$ space: (0.40, 14.52), (0.40, 15.88), (0.6, 16.28), and (0.6, 14.92). With the assumption that the clump populations in the whole bulge have the same properties as the one in the Baade's Window, the parallelogram described above can be shifted by the reddening vector to mark the expected locations of clump giants in different fields. The solid green lines are the boundaries of the region where one could find the clump giants in fields with different extinctions. The above justification serves only as a general guideline to the way the clump giants are selected. Several assumptions that went into creating this region should be carefully reviewed. For example, the assumed spread in V magnitudes can be either bigger or smaller or

[19]The $(V-R)_0$ color range given here is somewhat bluer than derived by Popowski et al. (2001a,b) and reported by Popowski et al. (2003a). The reason for this change is the detection of anomalous extinction law toward the bulge fields probed by microlensing surveys, which in turn affects the dereddened colors. A possibility of smaller than normal R_V coefficient in the bulge direction was suggested by Popowski (2000) and spectacularly confirmed by Udalski (2003) and Sumi (2004) based on the OGLE data. Very similar conclusions can also be drawn from the extinction calibrations derived by Popowski, Cook, & Becker (2003b) based on the MACHO data.

asymmetric around the central value, clump giants in different fields may have different characteristics etc.

A universal selection of clump giants outlined above (see also Popowski et al. 2001a, 2003a) allows some contamination by main sequence stars in high extinction areas of the sky. Popowski et al. (2001a,b) tried to remedy this problem introducing a universal color cut $(V-R) > 0.7$. However, the stars in high-extinction regions may become so red that the main sequence enters so-defined clump region from the blue. On the other hand, moving this generally fixed limit of $(V-R) = 0.7$ to the red would remove legitimate clump giants from low-extinction regions. Therefore, one is driven toward introducing a non-universal clump selection that makes use of the properties of the CMD at a given sky location.

At this point, it is important to understand why we are that particular about selecting an appropriate clump region. As mentioned earlier, the brightest stars in a given portion of the sky would not be seriously affected by blending. This statement applies well to both clump giants and bright main sequence stars that we try to eliminate. However, our goal is to select a clean sample of unblended *bulge* sources. The overwhelming majority of bright main sequence stars are in the foreground Galactic disk. Moreover, based on a CMD alone, it is very hard to distinguish bulge red giants from disk clump giants. Therefore, we decided to not include bright red stars in our clump sample. These two considerations limit clump giants to the relatively narrow strip associated with the extinction-based selection.

In our non-universal selection, we decided to keep our previous general procedure of selecting clump giants intact except for 1) the adjustments coming from the different form of the reddening-law adopted here, 2) addition of a blue color cut tied to the characteristics of the CMD. We checked that the region that is small enough to be sensitive to the local changes of extinction and large enough to form a reliable CMD approximately coincides with the, so-called, tile in the MACHO database. Each tile is a 4 by 4 arc-minutes patch and contains a few thousand identified stars. As our bulge fields contain more than 10000 tiles, it would be very impractical to define blue edges of clump regions on an individual basis. Therefore, we formed a training set of 240 tiles (in places corresponding to suspected microlensing candidates from the first 5 years of the experiment, but rejecting all tiles in 300 series fields and keeping only one copy of repeated tiles). This set of tiles is fairly representative and contains regions with a range of stellar densities and stellar extinctions. We decided to set a blue clump limit at $(V-R)$ half the way between the central clump and main sequence over-density at the V-magnitude of the clump. The 240 CMDs were visually inspected and the most likely clump boundary was selected. The next task was to relate these boundaries to the global properties of individual CMDs. We computed first four moments of the $(V-R)$ color of each CMD (no luminosity weighting). We used the mean and dispersion as the only parameters in the linear fit. Mathematically, we requested:

$$(V-R)_{\rm boundary} = \alpha + \beta\ \langle V-R\rangle_{CMD} + \gamma\, f\left(\sigma(V-R)_{CMD}\right), \quad (3)$$

where we tested three types of f(x), namely $f(x)=x$, $f(x)=x^2$, and $f(x)=\ln(x)$. All forms of equation (3) produced very similar results, and we adopted $f(x)=\ln(x)$, requesting that the clump giants be redder than:

$$(V-R)_{\rm boundary} = (-0.001\pm0.033) + (0.872\pm0.014)\ \langle V-R\rangle_{CMD} + (-0.042\pm0.012)\ \ln\left(\sigma(V-R)_{CMD}\right). \quad (4)$$

The errors reported in equation (4) were normalized to produce $\chi^2/d.o.f. = 1$.[20] The clump blue boundary determined by visual inspection that deviates most from the fit reported in equation (4) is at 3.28σ away. In general, the number of 3σ points is not very different than expected from a normal distribution of errors, and therefore we reject no points as outliers. Moreover, in the cases with largest deviations, the blue limits suggested by equation (4) are equally reasonable as originally selected boundaries, and, therefore, do not hint at any small subset of CMDs that do not obey a general relation. The average scatter of the visually-selected $(V-R)_{\rm boundary}$ around relation (4) is below 0.02 mag, which, being an order of magnitude smaller than a typical range of clump colors, is more than satisfactory.

Our final set of clump selection criteria are described by the following equations:

$$V_{\rm base} \geq 15.0 \quad \text{and} \quad V_{\rm base} \leq 20.5, \quad (5)$$

[20] The correlation matrix is:
$$\begin{pmatrix} 1.0000 & -0.9084 & 0.9720 \\ -0.9084 & 1.0000 & -0.7872 \\ 0.9720 & -0.7872 & 1.0000 \end{pmatrix}$$

$$V_{\rm base} \geq 4.2\,(V-R)_{\rm base} + 12.4, \quad (6)$$

$$V_{\rm base} \leq 4.2\,(V-R)_{\rm base} + 14.2, \quad (7)$$

$$(V-R)_{\rm base} > (V-R)_{\rm boundary}, \quad (8)$$

$$\text{field} < 300 \quad \text{or} \quad \text{field} > 311, \quad (9)$$

where subscript "base" referring to V-magnitude and $(V-R)$-color indicates baseline magnitudes, i.e. the ones in the limit of no microlensing-induced amplification. The cut on bright sources in (5) is intended to eliminate events that are in the foreground or may have saturated photometry, the cut on faint sources is designed to avoid stars with uncertain photometry or highly affected by blending. In practice, the cut on bright sources from (5) is always weaker than the combination of cuts (6) and (8). Cuts (6) and (7) determine the reddening channel that marks the possible locations of clump giants. Cut (8) admits only stars with red enough color, which removes contamination by foreground main sequence stars. Finally, cut (9) excludes 11 disk dominated/contaminated fields, namely the ones in the 300 series.

The slope of relations (5) and (6) has the interpretation of the coefficient of selective extinction $R_{V,VR} \equiv A_V/E(V-R)$. The coefficient we use here $R_{V,VR} = 4.2$ was found by Popowski et al. (2003b) in Baade's Window. We checked that clump selection based on $R_{V,VR} = 4.5$ produces very similar results. On the other hand, $R_{V,VR} = 5.0$ seems to be too steep. Despite this, Popowski et al. (2001a) selection was quite successful, because their intrinsic clump color was assumed to be redder and they had very few events in high-extinction regions, which are primarily affected by this change. The properties of extinction law and the zero-point needed to determine absolute extinction in the bulge are not known precisely. However, even if the dereddened color range of clump giants in the Baade's Window is different than assumed here it does not mean that the selection of clump giants is biased. We checked in the number of regions with different level of reddening that the operational procedure defined in equations (5)-(9) properly picks up clump giants in a wide range of color-magnitude diagrams.

Clump region defined by conditions (5)-(9) is plotted in Figure 3 and surrounded by bold green lines. In addition to the boundary of clump region, we also indicate cut (5) by blue lines, cuts (6) and (7) by red lines, and cut (8) by dotted magenta line, with arrows indicating its non-universal, CMD-specific character. The clump events are marked as filled triangles. The

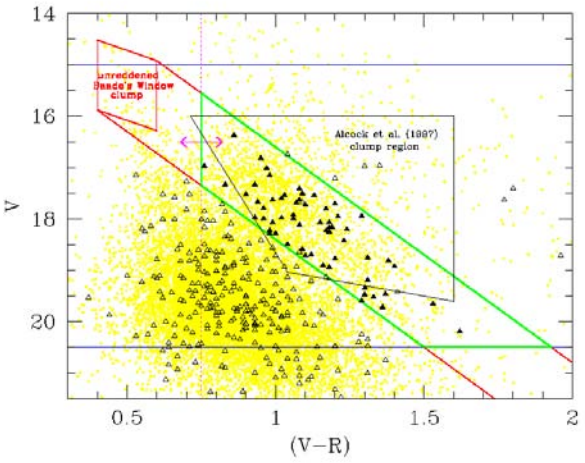

Fig. 3.— Color-magnitude diagram of MACHO objects. Triangles are events and filled triangles are clump events. The underlying population is shown in yellow.

events inside bold green lines marked as open triangles belong to fields in 300 series, and are excluded by cut (9). Alcock et al. (1997a) clump region is presented for comparison.

The properties of the 62 lensed clump giant stars as well as the microlensing fit parameters are given in Tables 2 and 3. In these and the following tables V and $(V-R)$ will refer to baseline magnitudes – we drop subscript "base" to avoid clutter. We note that two events are marked with letters ('a' or 'b') indicating they are duplicates of another event (duplicate also marked 'a' or 'b'). In general, this is caused either by the same physical event being detected in an overlapping field, or by a nearby star receiving flux from the actual event due to incorrect flux sharing in the photometric PSF fitting code. Both duplicate events listed in Tables 2 and 3 result from field overlaps. For the optical depth calculation we will count both of the duplicate events since field overlaps increase both the total number of stars monitored and the number of events detected proportionally, and since the field overlap and number of duplicates is fairly small. Finally we note that 6 of the clump giant microlensing events are potential binary events, marked with a ‡ symbol. We must carefully treat these when calculating the optical depth.

In Figure 4 we graphically summarize the basic properties of clump events. Most of the panels are

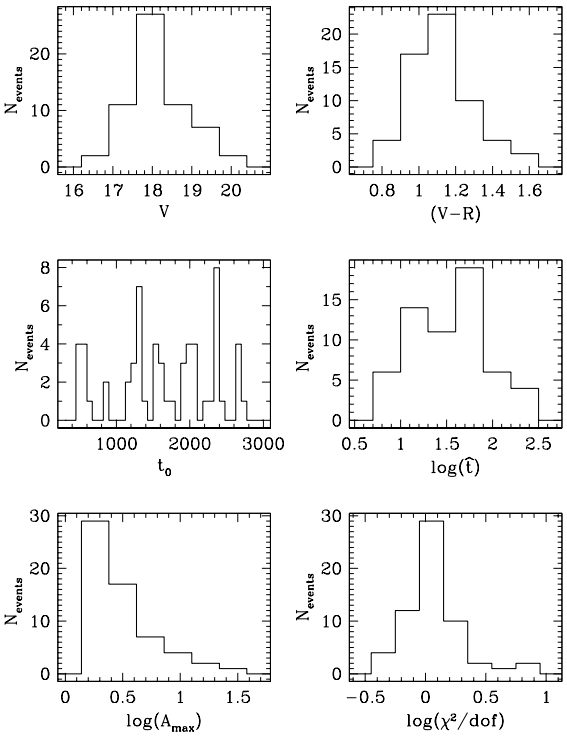

Fig. 4.— Basic properties of the clump sample.

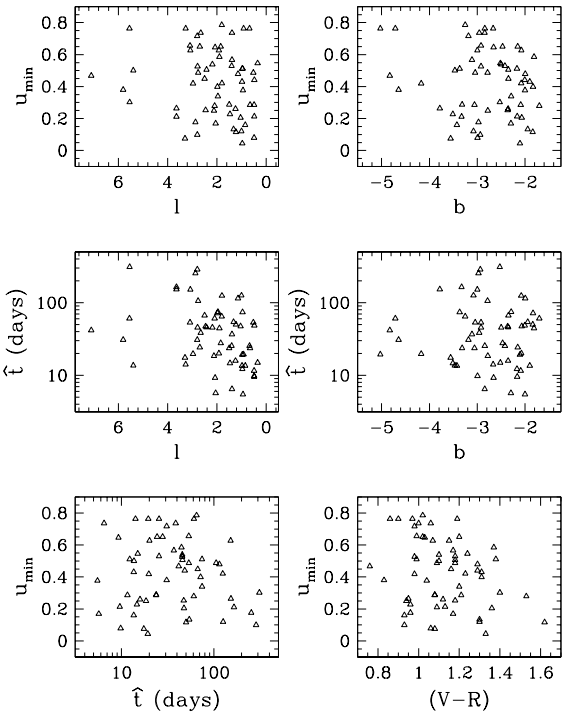

Fig. 5.— Microlensing properties of events as a function of position, duration, or color.

self-explanatory. Let us only remark about the distribution of the number of events versus the time of maximum amplification t_0. The peaks in the histograms show 7 observing seasons analyzed here. The number of detected events varies mostly due to Poisson noise with the noticeable exceptions of the second and last seasons. The numbers of events are particularly low there due to an observing strategy that targeted very few fields in search for short-duration events.

In Figure 5 we test for possible systematic effect in microlensing parameters. In particular, in the upper four panels we plot impact parameters and Einstein diameter crossing times as a function of Galactic coordinates. One sees no dependence of parameters upon position. The left lower panel suggests that there is no correlation between the impact parameter and duration, and the right lower panel shows that the impact parameter is not related to the event color.

Finally, we note that many of the events selected here were alerted on by us earlier in the experiment. In addition, the MACHO fields overlap with fields from other microlensing experiments. We cross-referenced the clump sample with our own alert events and with events from EROS, MOA, and OGLE experiments. We found no counterparts in the MOA set (as expected from non-overlapping observing seasons). Alternative designations from the MACHO Alert system and counterparts from EROS and OGLE are listed in Table 4.

4. Is Blending Negligible for the Clump Sample?

To check whether the sample of selected clump giants meets our expectations of being unaffected by blending we applied several tests.

First, we checked the color light curves of all events with particular emphasis on the peak region. The light curves of all clump events showing blue and red magnitudes and the difference between them for simultaneous observations are shown in Figure 6. Here we display two example events, whereas the entire sample is available in the electronic version and will be

available on the World Wide Web upon the acceptance of this paper[21]. The red lines superposed on the data are the best fits obtained under the assumptions of no blending, and in most cases they properly represent observational points. We examine the light curves for any deviations from the unblended fits. We note that events 109.20640.360, 113.19192.365, 176.18826.909, 401.47994.1182, 401.48052.861, 401.48167.1934, 402.47856.561, and 403.47491.770 either lack or have extremely sparse color coverage in the peak region. Therefore, any blending-related information that can be extracted from their light curves is very limited. The events for which there is at least a slight possibility of achromatic signal are listed in Table 5. Several events have deviation from fitted light curves that are due to their exotic character: either binarity or parallax effect. Only 10 out of 62 events are not immediately explained by known effects. In addition, 3 of them have either asymmetric or caustic type signal which is more likely an indication of their binary character than blending. Therefore, only 7 events (11%) can be suspected of significant blending based on the visual inspection of their light curves.

Next we examined the color close to the center of the peak ($t - t_0 < \hat{t}/\sqrt{2}$) compared to the baseline of the lightcurve in a more quantitative fashion. We start with a region of width $\hat{t}/8$ centered on t_0 and expand it until we have at least 2 points with simultaneous observations in each filter. Using these points in each lightcurve we calculate the difference in flux between the peak and the baseline in each filter (ΔV or ΔR). In Figure 7 we plot the ratio $\Delta V/\Delta R$ versus $A_{\max}$. For blending-free microlensing events $\Delta V/\Delta R$ should be unity since gravitational lensing is wavelength independent. Of the 53 events that had simultaneous observations in both filters in the peak, 20.7% were more than 1σ away from unity. This is consistent within errors with no blending in our sample. There are two events (108.18951.593 and 403.47610.576) which differ by more than 6 sigma from unity, which might be indicative of blending. One (108.18951.593) is likely blended with a faint star of a very different color, and examination of the lightcurve of the second one shows that it has many points far off the microlensing fit (403.47610.576), probably indicating intrinsic variability or problems with the photometry of this star. If we ignore these two events we have 17.6% more than 1σ from unity and the distribution is roughly Gaussian.

[21] See `http://wwwmacho.mcmaster.ca`

As our third test, in Figure 8, we plot the cumulative distribution of the impact parameters $u_{\min}$ and a uniform distribution (straight line) of $u_{\min}$ between 0 and 0.826. This distribution is what is predicted for microlensing events with magnifications between infinity and 1.5 as imposed by our selection criteria. We find good agreement, with the Kolmogorov-Smirnov $D = 0.101$ for 60 events. Under the hypothesis that all events are microlensing, this gives a probability of 55% of obtaining a value of D this large or larger. For this analysis we made a correction for the efficiency of each event, but even without making this correction we get excellent agreement ($D = 0.081$ for a probability of 81%). This suggests that $u_{\min}$ values from standard microlensing fits are not seriously biased by blending.

Finally, we perform so-called blend fits. That is we fit every flux curve with a formula

$$F(t) = F_{\rm base}\left[(1-f) + fA(t)\right], \qquad (10)$$

where $A(t)$ is the amplification of standard point lens microlensing, $F_{\rm base}$ is the baseline flux of an object unaffected by the microlensing magnification, and f is the blending fraction. The blending fractions for an event can take different values in blue and red filters. For a completely unblended source $f = 1$ is expected. We fit all curves using MINUIT (CERN Lib. 2003), and report the results together with the parabolic errors in Table 6. The distribution of blend fractions for all unique clump events excluding binaries is presented in Figure 9. As expected, many events have blend fractions close to 1.0, i.e. consistent with no blending. At the same time, however, the results look very alarming. There is a number of events with small blend fractions that indicate heavy blending. Therefore, we investigate the blending issue for events where a blend fit produced a lower χ^2/dof than a standard fit. The distribution of their blend fractions is illustrated in the upper panel of Figure 10. To understand the meaning of this result we start with Monte Carlo simulations of the expected distribution of recovered blend fractions for *completely unblended* clump events from a sample identical to the one presented in the upper panel of Figure 10. We create light curves of unblended events with durations and $u_{\min}$ values identical to the ones from the real sample. We produce a few hundred light curve realizations for each event and compute for them blend fit parameters. Thus for each real event we obtain an expected distribution of recovered blend fractions if the original event was unblended. We sum those distributions together to obtain the ex-

pected blend fraction distribution for the real sample. We plot the resultant distribution in the lower panel of Figure 10. Therefore, even if there is no blending in our clump sample, the blend fit procedure will predict many blended events. This problem has been studied before and is a result of sampling and data quality (Woźniak and Paczyński 1997). The shapes of the distributions from Figure 10 are similar, which suggests that our null hypothesis that the clump sample is unblended may be correct. However, we also note that the real sample seems to have some excess of events with very small blend fractions.

To further test possible contamination of the clump sample by highly blended events, we notice that the blending fractions themselves do not tell the entire story. There is no reason to reject a non-blending hypothesis as long as the blend fractions are consistent with f = 1. Therefore, we compute the deviation δ of a blend fraction from f = 1 in units of the error in the blend fraction:

$$\delta = \frac{f - 1.0}{\sigma_f}, \tag{11}$$

where δ assumes negative values for $f < 1.0$ and positive values for $f > 1.0$.[22] It is obvious from the definition that δ will not significantly differ from 0 for events consistent with no blending. The events with large deviations can be classified as suspicious. We plot the distributions of $\delta_{\rm blue}$ for the real and simulated samples in Figure 11. Again, the distributions are not very different from each other, but we cannot exclude the possibility of significant blending for some events in our original sample of 60 unique clump events. We conclude that, given the quality of our data, the blend fit parameters we find for events with a single lens are not very useful in determining the amount of blending in our sample. Nonetheless, since our ultimate goal is to obtain a reliable estimate of the optical depth, we use blend fit results to select a subset of our sample, which we design to be fully consistent with no blending. This extremely conservative subset consists only of the events with $|\delta_{\rm blue}| < 2.0$. It is encouraging that this subsample contains very few events from Table 5. The analysis of this verification sample conducted in the next section will provide an essential check on the systematic error in our primary optical depth determination based on the entire clump sample assumed to be blending-free.

Finally, we notice that blending fits to events with binary lenses are substantially better constrained than the fits to events with single lenses. Our clump sample contains 4 binaries that have been previously analyzed by Alcock et al. (2000c): 108.18951.593 (97-BLG-28), 118.18141.731 (94-BLG-4), 401.48408.649 (98-BLG-14), and 402.47864.1576 (97-BLG-41). The first three have fits in Alcock et al. (2000c, Table 3). Out of 16 bulge binaries that have blend fits in Alcock et al. (2000c) only 6 are fully consistent with no blending (94-BLG-4, 96-BLG-4, 97-BLG-1, 97-BLG-28, 98-BLG-14 ("dashed solution"), and 108-E). On the other hand, the three *clump* binaries for which we have fits have blend fractions very close to 1 and are consistent with no blending (see their blend fractions in Table 7). The probability that the clump binaries share the same blending characteristics as the entire sample of binaries is $P(3) \equiv \binom{3}{3}(6/16)^3(10/16)^0 = 0.053$. Therefore, we have a $2\,\sigma$ indication that our clump sample may be affected by blending to negligible extent.

5. The Optical Depth

We propose to use an estimator of the optical depth which is different from, but closely related to, the one we used previously. The estimator used in our previous papers is:

$$\tau = \frac{\pi}{4E} \sum_{i=1}^{N_{\rm events}} \frac{\hat{t}_i}{\epsilon(\hat{t}_i)}, \tag{12}$$

where $\hat{t}$ is time to cross the Einstein ring diameter, E is the total exposure in star-days (equal to the number of stars times time span of observations), and $\epsilon(\hat{t})$ is an efficiency for detecting an event with a given $\hat{t}$.

A formula which gives the same answer in the limit of large numbers of events, but which we find more computationally efficient is:

$$\tau = \frac{1}{E} \sum_{i=1}^{N_{\rm events}} \frac{t_i}{\epsilon(t_i, A_{{\rm max},i})}, \tag{13}$$

where t_i is the measured time for which the magnification is above $A = 1.34$, that is the time the line-of-sight is within the Einstein ring radius. Appendix A gives the derivation of both of these formulae and makes the case for the use of equation (13). Note that due to our cut $A_{\rm max} \geq 1.5$, we must multiply the value

[22] The blend fractions with $f > 1.0$ seem unphysical, but they can result from local fluctuations in the sky level. Such fluctuations will typically produce $f \lesssim 1.2$, but even $f > 1.2$ solutions should not be rejected as long as they are consistent with physically motivated f values. All solutions in our sample meet this basic condition.

derived from equation (13) by a correction factor of 1.09. This is explained in Appendix A.

There are six likely binary events in our sample. Not only is the parameter determination more difficult in their case, but our detection efficiency pipeline described below is designed for the events with a single lens. Therefore, it is not immediately clear how to include binaries in the analysis. They cannot be simply omitted because this would lead to an underestimate of the optical depth. For simplicity we used for binaries t_i as found from single lens fit. We found this quite accurately measured the time above $A = 1.34$, and agrees quite well with what is found from the binary lens fits (Alcock et al. 2000c). We notice that the values of $\hat{t}$ found from the single lens fits are not very useful for these events.

The sampling efficiencies were obtained with the pipeline that has been previously applied to the LMC data (for a description see Alcock et al. 2000b). In brief, a random subset of 1% of all lightcurves was selected and artificial microlensing light curves with different parameters were added to these lightcurves. Then the same analysis used to select real events was applied to this set. Efficiencies were computed as the number of events recovered divided by the number of events input as a function of both the input duration and the input maximum magnification of the input event. Since the number of clump giants in each 1% sample field is not large, several passes were made through each 1% data base, until enough statistics were gathered. We averaged over $A_{\rm max}$ to report efficiencies for each field as a function the event duration ($\hat{t}$), and we also did special runs using the measured t_i and $A_{{\rm max},i}$ for each real clump giant microlensing event. This last analysis gave us $\epsilon(t_i, A_{{\rm max},i})$ for use with t_i in equation (13) above. Figure 12 shows the results of our efficiency calculations for the fields with events, and Table 3 shows the efficiency calculated for each event. Relative sampling efficiencies for all 94 bulge fields are given in Table 8. The results in fields in the 300 series are not used in the optical depth analysis and they may be affected to higher extent by systematic effects.

Using the above method and the clump events from Table 3, we present in Table 9 optical depths for each field that contains clump giant events. The center position of each field, the number of clump giant source stars (in the text designated shortly by N_f), and the number of recovered microlensing events are also given. The number of days, $T_{\rm obs} = 2530$, used to find each field's exposure $E = N_f T_{\rm obs}$ was set by the efficiency calculation[23]. Since the number of events in each field is so small the error in the optical depth is dominated by Poisson statistics. We compute these errors using the formula given by Han & Gould (1995).

We show in Figure 13 the spatial distribution of optical depths on the sky. In the left panel we give the optical depth value at the center of each field with clump events, and in the right panel we present the color representation of the same results and indicate the number of detected events. We note the anomalous character of field 104, with an optical depth of $(8.8 \pm 3.7) \times 10^{-6}$, almost two sigma above the average. The results for individual fields are very uncertain but taken as an ensemble they suggest that the optical depth has a substantial gradient in Galactic latitude. This property is more apparent in Figure 14, where we binned the data on a 0.5 deg scale in the b-direction and 1.0 deg scale in the l-direction. Based on 57 clump giant events selected from observations of the 1260000 clump giant source stars within 5.5 degrees of the Galactic center we find the optical depth gradient of $(1.06 \pm 0.71) \times 10^{-6}{\rm deg}^{-1}$ in the b-direction and $(0.29 \pm 0.43) \times 10^{-6}{\rm deg}^{-1}$ in the l-direction.

Many fields do not contain any clump events. In those cases we derive an upper limit on the optical depth from

$$\tau_f^{\rm lim,CL} = \nu^{\rm CL} \left(\frac{\pi}{4 N_f T_{\rm obs}} \frac{\sum_{i=1}^{N_{\rm events}} \hat{t}_i / \epsilon_i(\hat{t}_i)}{\sum_{i=1}^{N_{\rm events}} \epsilon_f(\hat{t}_i) / \epsilon_i(\hat{t}_i)} \right), \quad (14)$$

where ϵ_f is the efficiency in field f, ϵ_i is the efficiency for i-th event in its field of origin, and $\nu^{\rm CL}$ is the multiplication factor dependent on the confidence level. Equation (14) is derived in Appendix B. We use $\nu^{1\sigma} = 1.8379$ when we compute the upper limits on the optical depth given in Table 10. Those upper limits were computed without any direct reference to the Galactic model. However, they rely on the assumption that the intrinsic duration distribution in empty-fields is identical to the one in fields with events, and this approximation can break down for some Galactic models. In addition, let us note that the limits from Table 10 are rather conservative in the sense that the true values may be lower. This is caused by the fact that we used durations of all events when we applied equation (14). We show in the next section that field

[23] The number of days $T_{\rm obs}$ is equal to the sum of the allowed t_0 span ($2850d - 419d = 2431d$) and two ~ 50-day buffer regions added at the beginning and the end of the observing interval.

104 tends to have longer events. If events in field 104 were excluded from the summation in equation (14), then the limits would go down a little.

Since the number of events in individual fields is typically very small, microlensing studies customarily give average optical depth based on many fields to beat the Poisson noise. The main problem with this approach is the fact that the interpretation of the average optical depth and position is difficult due to non-linear variations of τ over the area of the survey. Decreasing the size of the region for averaging results in reappearance of the Poisson noise issue. Here we deal with these competing effects by selecting a very compact region that contains 2/3 of all clump events. We call this region Central Galactic Region (CGR) to stress its close proximity to the Galactic center (but we would like to clarify that there are no MACHO fields that include the Galactic center itself). CGR covers about 4.5 sq. degrees and is composed of 9 fields: 108, 109, 113, 114, 118, 119, 401, 402, 403. Using 42 events in CGR, we find an average optical depth of $\tau_{\rm CGR} = 2.17^{+0.47}_{-0.38} \times 10^{-6}$ at $(l, b) = (1.^{\circ}50, -2.^{\circ}68)$ [24]. For this set of fields, an exposure is $E = 1.869 \times 10^9$ star-days (2530 days times 738850 clump giant stars). In this case the error was found by Monte Carlo simulations as described by Alcock et al. (1997b), and is somewhat larger than the simple Poisson error (which would be $\pm 0.34 \times 10^{-6}$), but consistent with the formula of Han and Gould (1995), which gives $\pm 0.42 \times 10^{-6}$. We note that the result found using equation (12) and an interpolated efficiency as a function of $\hat{t}$ is nearly identical ($2.16^{+0.46}_{-0.38} \times 10^{-6}$). Field 104, with the largest optical depth, falls just outside of the CGR. To test how sensitive the results are to the detailed shape of the region selected for the determination of the average optical depth, we create a rectangular region "CGR+3", which is composed of CGR plus the three adjacent fields at the same galactic latitudes (fields: 176, 104, 105). The optical depth in such an extended region is $\tau_{\rm CGR+3} = 2.37^{+0.47}_{-0.39} \times 10^{-6}$ at $(l, b) = (1.^{\circ}84, -2.^{\circ}73)$, entirely consistent with our principal result. Also, we note for completeness that when we use all 2.44 million clump giants and all 62 events the optical depth over all 83 analyzed fields is: $\tau_{\rm all} = (1.21 \pm 0.21) \times 10^{-6}$ at $(l, b) = (3.^{\circ}18, -4.^{\circ}30)$, but this number is hard to interpret given non-linear (and often rapid) variations of the optical depth with Galactic position mentioned earlier.

Finally, we return to the question of blending and its effect on the optical depth. To test the sensitivity of the optical depth to possible systematic errors, we analyze the verification sample of events. To avoid possible systematic errors we first exclude all binaries. Then we keep only the events that have $|\delta_{\rm blue}| < 2.0$, which makes them very consistent with no blending. We list the events that pass this additional cut in Table 11. We list events that belong to CGR on the left and the events in the other fields on the right.

The analysis on this sample proceeds in a fashion that is similar to the main analysis but has a noticeable difference. Our verification sample is constructed by utilizing the cut that uses blend fit results. Applying the same procedure to our massive efficiency simulations is beyond the scope of this paper. Therefore, we use the previously determined efficiencies and the following estimator of the optical depth:

$$\tau^{\rm ver} = \frac{N^{\rm orig}_{\rm events}}{N^{\rm ver}_{\rm events}} \left(\frac{1}{E} \sum_{i=1}^{N^{\rm ver}_{\rm events}} \frac{t_i}{\epsilon(t_i, A_{{\rm max},i})} \right), \quad (15)$$

where $N^{\rm orig}_{\rm events}$ and $N^{\rm ver}_{\rm events}$ are the numbers of events in a given field or region counted in the original and verification sample, respectively. In designing the optical depth estimator given in equation (15) we assumed that blending (or other systematic effect we would like to test) does not change the number of detected events, but it may substantially affect the event parameters and may render the sampling efficiencies inappropriate. However, both the parameters and efficiencies can still be used for the verification sample. The factor $N^{\rm orig}_{\rm events}/N^{\rm ver}_{\rm events}$ is introduced to compensate for the fact that we remove some events without replacing their optical depth contributions with anything else.

The optical depth values in individual fields derived using equation (15) for our verification sample are given in Table 12. The first four columns give the field number, $N^{\rm ver}_{\rm events}$, the optical depth derived using equation (15), and its error. For comparison, columns 5 and 6 give $N^{\rm orig}_{\rm events}$ and the optical depth based on equation (13) derived earlier. The results from the verification sample agree very well with our previous estimates. As the last step we limit the verification sample to the CGR[25]. The average optical depth based on this verification sample of 22 events

[24] The unweighted average position for 9 CGR fields is $(l, b) = (1.^{\circ}55, -2.^{\circ}82)$

[25] It may seem surprising that only 61% or 22 events out of 36 non-

is $\tau_{\rm CGR}^{\rm ver} = 2.42^{+0.75}_{-0.58} \times 10^{-6}$, in excellent agreement with our main result.

In summary, we see no evidence that our optical depth results are strongly affected by blending. There are two likely explanations of why this is the case. First, it is possible that the clump sample is to a large extent unaffected by blending. Second, substantial blending is a result of a large number of unresolved sources. In such situation, the bias in the recovered event duration is countered by the bias in the inferred number of sources. At the moment, we do not have enough information to distinguish between these two possibilities, but our optical depth determination benefits from their fortunate properties.

6. Clustering of Events and Concentration of Long Events in Field 104

The optical depth for field 104 is larger than any other field and we would like to investigate whether this is a statistical fluctuation or an indication of something unusual about this region of the Galaxy. The large optical depth is related to the fact that 9 of the 62 clump giant events are in field 104, and because there is also a high concentration of long-duration events in this field. Four out of the 10 events longer than $\hat{t} = 100$ days are in field 104, including the 2 of the 3 longest.

We investigate how statistically significant this concentration is. We do not account for the change in the detection efficiency of events with different durations in different fields, so we place only a lower limit on significance of the difference between duration distributions in field 104 and the others. The efficiency for detecting long events is similar in most fields with events observed for 7 years, because this does not depend strongly on the sampling pattern. The detection of short events will be lower in a sparsely sampled fields. Therefore, the number of short events in some of the fields used for comparison may be relatively too small with respect to a frequently-sampled field 104, but this is only going to lower the significance of the $\hat{t}$ distribution difference computed here. In conclusion, the analysis of event durations *uncorrected* for efficiencies should provide a lower limit on the difference between field 104 and all the remaining clump giant fields.

For the significance test, we use the Wilcoxon's number-of-element-inversions statistic. First, we divide events into two populations: events in field 104 and all the remaining ones. We test two types of possible separations into those two populations: A. we select all events in field 104 to the first sample (9 events) and all the remaining events except duplicates from field 109 to the second sample (51 events), B. we select all events in fields 104 and not in any other field to the first sample (7 events) and all the events in the remaining fields the second sample (53 events). In both cases the entire sample of 60 unique clump giants can be recovered as the sum of populations in 104 and not in 104.

Case A and B are then each tested separately according to the following procedure. We order the events in the combined sample of two populations from the shortest to the longest. Then we count how many times one would have to exchange the events from field 104 with the others to have all the 104 field events at the beginning of the list. If N_1 and N_2 designate numbers of elements in the first and second sample, respectively, then for $N_1 \geq 4$, $N_2 \geq 4$, and $(N_1 + N_2) \geq 20$, the Wilcoxon's statistic is approximately Gaussian distributed with an average of $N_1 N_2/2$ and a dispersion σ of $\sqrt{N_1\, N_2\, (N_1 + N_2 + 1)/12}$.

In case A, the Wilcoxon's statistic is equal to 324, whereas the expected number is 230 with an error of about 48. Therefore the events in 104 differ (are longer) by 1.96σ from the other fields. In case B, the Wilcoxon's statistic is equal to 282, whereas the expected number is 186 with an error of about 43. Therefore the events in 104 differ (are longer) by 2.22σ from the other fields. Both divisions of the clump sample into field 104 and the remaining fields lead to the conclusion that events in fields 104 are inconsistent at the 2 σ level with being drawn from the same parent population as events in the remaining fields. We obtain similar discrepancy between the time scales of events in field 104 and the remaining fields when we use all 318 unique events from selection criteria C listed in Table 3 of the companion paper. This result is somewhat less significant than the one derived by Popowski et al. (2001a). We note, however, that similar analysis of an almost independent Alcock et al. (2000a) DIA sample also suggests anomalous character of duration distribution in field 104 (Popowski 2002). We conclude that the unusual character of field 104 should be

binary events in the CGR pass $|\delta_{\rm blue}| < 2.0$ cut. We note however that the corresponding ratio for our simulated *unblended* sample from the lower panel of Figure 11 is 74%. This slight difference is easily explained by the fact that the Monte Carlo simulations do not include exotic events (e.g., parallax events) which are present in the real sample and can cause the blend fits to falsely indicate blending.

investigated with additional observations but we cannot completely exclude the possibility that this effect is due to a statistical fluctuation.

In addition, there seem to be clusters of events (of all durations) on the sky in fields 104, 108, and 402. If microlensing events are clustered on the sky above random chance it has important consequences. It could indicate clustering of lenses, perhaps in some bound Galactic substructure or very young star forming region. The long duration of the events could indicate that the substructure contained heavier objects such as black holes. Alternatively, it could indicate a concentration of orbits through the Milky Way and a place where the orbital speeds were slower than normal.

In order to test the significance of the apparent clustering of microlensing events we devised a Monte Carlo test in which we simulated 10000 microlensing experiments each detecting 60 unique clump giant events. In each experiment we found densest cluster of 3 events and the densest cluster of 4 events and recorded the radius of the cluster. We then compared the radii of the densest 3-cluster and densest 4-cluster in the actual data to the density distributions formed by our Monte Carlo experiments. This gives us the probability of finding by chance a 3-cluster (or 4-cluster) as small as we found in the actual data. In both the data and in the simulations we remove any star that is found two or more times (e.g., in an overlap region), since these give a false measure of dense clustering.

In performing the simulations we selected 60 clump giant stars at random from the 1 percent data base so that the distribution of lensing sources matched that in the data. We also weighted each event by the 50-day efficiency of that field (Table 8), so that fields with low sampling efficiencies were properly underrepresented. Finally we considered various gradients in optical depth across our fields. As one limit we use a uniform optical depth across our fields and as the other we use a steep linear gradient which results in the optical depth changing from a maximum at the Galactic center to 0 at $|b| = 4^\circ$. This later case, is roughly consistent with, but somewhat steeper than, the gradient shown in Figure 14. The actual gradient should be between these two extremes. The second case increases the chance of randomly finding a cluster with respect to the first case.

With no optical depth gradient we find a probability of 1.9% of finding a 3-cluster as dense as in the data, and 4.6% of finding a 4-cluster this dense. For the steep optical depth gradient, we find probabilities of 8.7% and 27% respectively. Unfortunately these results are not very conclusive. The clustering of microlensing events we find in our data is marginally significant, but certainly not compelling.

We also performed the clustering analysis on the entire sample of 318 unique microlensing events selected with criteria "C". For uniform optical depth the probability of finding a 3-cluster as dense as in the data is 7.3% and the probability of finding a 4-cluster this dense is 3.6%. For the steep optical depth gradient the probabilities are 36% and 32% respectively. So for the entire sample of microlensing events we find no strong evidence of clustering on the sky.

7. Conclusions and Discussion

Using 7 years of MACHO survey data, we presented a new determination of the optical depth to microlensing towards the Galactic bulge. We selected the sample of 62 microlensing events (60 unique) on clump giant sources (out of more than 500 total) and performed a detailed efficiency analysis. Using a subsample of 42 clump events concentrated in just 4.5 deg^2, we found $\tau = 2.17^{+0.47}_{-0.38} \times 10^{-6}$ at $(l, b) = (1.^\circ 50, -2.^\circ 68)$, consistent with theoretical expectations.

We can make a comparison with previous MACHO collaboration measurements by using our current clump sample in the fields analyzed previously. For example in the 24 fields used by Alcock et al. (1997a), we find 37 clump events giving $\tau = 1.36^{+0.35}_{-0.28} \times 10^{-6}$, which is two sigma below the earlier result of $\tau = 3.9^{+1.8}_{-1.2} \times 10^{-6}$. Over the 8 fields in our difference imaging study (Alcock et al. 2000a), our current, almost independent sample gives $\tau = 2.20^{+0.67}_{-0.52} \times 10^{-6}$ at $(l, b) = (2.^\circ 68, -3.^\circ 35)$, which is in good agreement with that earlier result of $\tau = 3.23^{+0.52}_{-0.50} \times 10^{-6}$ (and with even better agreement with the DIA result uncorrected for the fudge factor discussed in the Introduction).

Our new value of $\tau_{\rm CGR} = 2.17^{+0.47}_{-0.38} \times 10^{-6}$ is also very consistent with the recent EROS collaboration (Afonso et al. 2003) measurement. They found $\tau = (0.94 \pm 0.29) \times 10^{-6}$ at $(l, b) = (2.^\circ 5, -4.^\circ 0)$ from 16 clump giant events and an efficiency calculation similar to ours. The values are different but they are reported at different position. The difference becomes entirely insignificant if we take into account either the numerical value of the gradient reported in §5 or read off the approximate optical depth value at $b = -4.0$

from Figure 14. In addition, our new optical depth is in very good agreement with recent theoretical prediction of the Galactic bulge optical depth ($\tau = 1.63 \times 10^{-6}$) by Han & Gould (2003).

We note that about 41% of the optical depth is in the events longer than 100 days (10 out of 62 events), and about 63% of the optical depth is in events longer than 50 days (21 out of 62 events). This may be at odds with some models of the Galactic structure and kinematics (e.g., Han & Gould 1996), but consistent with others (Evans & Belokurov 2002) which include streaming motion along the bar. The distributions of event durations are shown in Figure 15 where we plot histograms for uncorrected and efficiency-corrected cases. We note that the mean Einstein diameter crossing time of all our clump giant events is $\langle \hat{t} \rangle = 56 \pm 64$ days and for our fields close to the Galactic center $\langle \hat{t} \rangle_{CGR} = 39 \pm 31$ days. To facilitate proper comparison with theoretical models we have to weigh each event by its inverse efficiency (Table 3). Then the averages become: $\langle \hat{t} \rangle\,(\mathrm{eff}) = 40 \pm 50$ days for all fields and $\langle \hat{t} \rangle_{CGR}\,(\mathrm{eff}) = 30 \pm 29$ days for fields in the CGR[26]. Evans & Belokurov (2002) find average Einstein crossing times range from around 100 days in models that include bar streaming motion to 30 days in models without bar streaming. Our values are too uncertain to distinguish between these kinematic possibilities and are consistent with both types of models.

KG and CT were supported in part by the DoE under grant DEFG0390ER40546. DM is supported by FONDAP Center for Astrophysics 15010003. This work was performed under the auspices of the U.S. Department of Energy, National Nuclear Security Administration by the University of California, Lawrence Livermore National Laboratory under contract No. W-7405-Eng-48.

[26] Because the distribution is non-Gaussian we also give the median and quartiles, which are (23.7, 12.0, 47.8) for all clump events and (18.7, 9.5, 46.9) for clump events in the CGR.

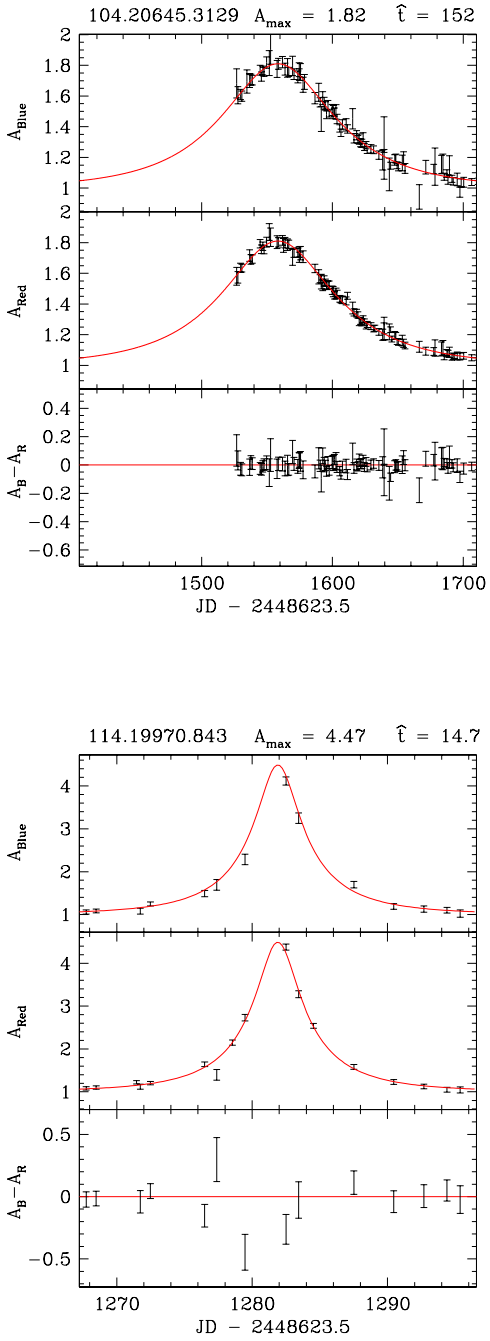

Fig. 6.— The upper panel shows the event with no color signal, and the lower panel the event with a weak signal. On each panel, the upper box shows the amplification in the blue filter (the baseline flux has $A = 1$), the middle box the amplification in the red filter, and the lower box the difference between the two which is an indication of color. Shown are only the peak regions within $\hat{t}$ of the time with maximum amplification t_0.

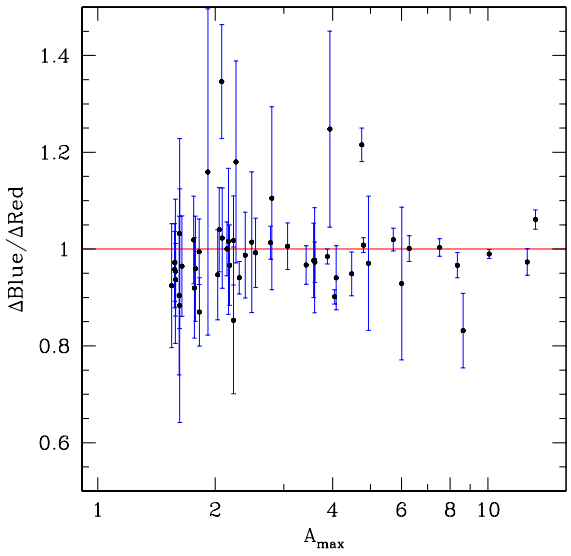

Fig. 7.— Ratios of $\Delta V/\Delta R$ for the 53 events with observations in the peak of the lightcurve.

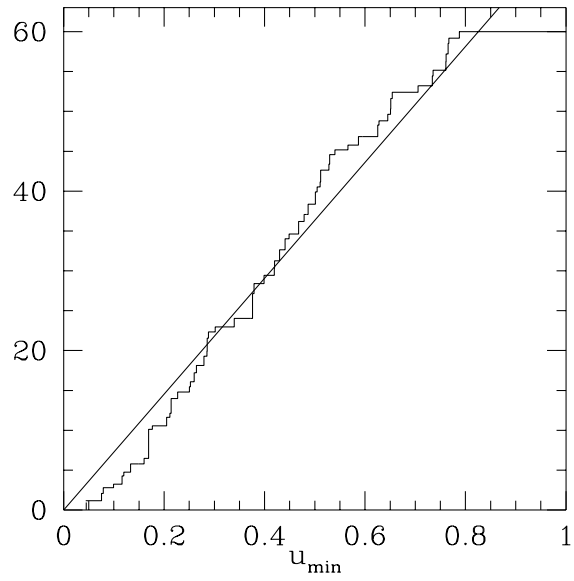

Fig. 8.— Cumulative distribution of impact parameters weighted by inverse efficiencies (renormalized to 60, the total number of unique clump giant events). Our cuts limit the impact parameter to 0.826.

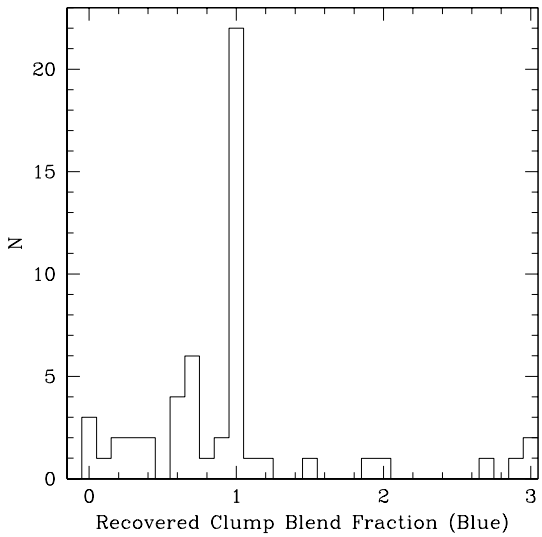

Fig. 9.— The distribution of blend fractions (blue) for the entire clump sample excluding binaries.

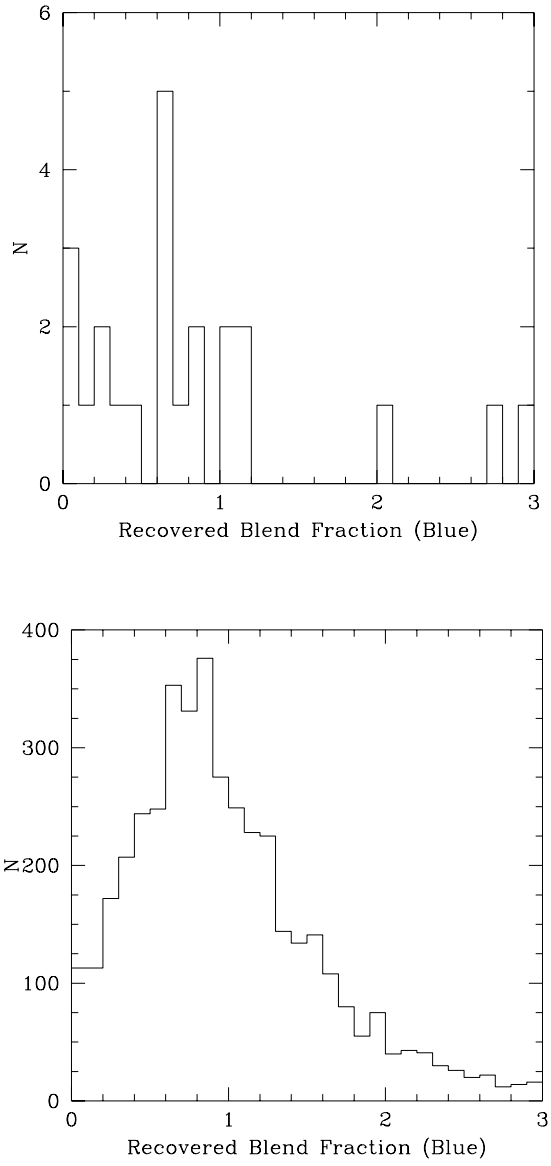

Fig. 10.— Upper panel presents blue blend fraction distribution for the clump sample from CGR (see §5). Eleven events from CGR are better fit without blending and left out of this plot. The lower panel shows blend fractions for the sample of simulated unblended events.

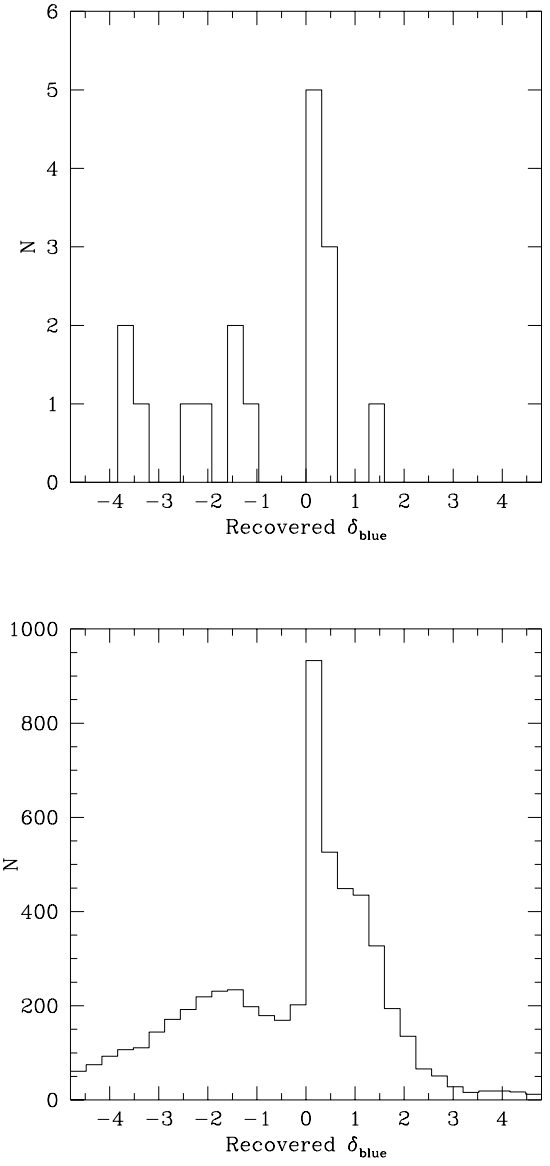

Fig. 11.— Upper panel presents the distribution of δ in blue filter for the clump sample from CGR (selected in the same way as for Figure 10). The lower panel shows the corresponding histogram for the simulated unblended events.

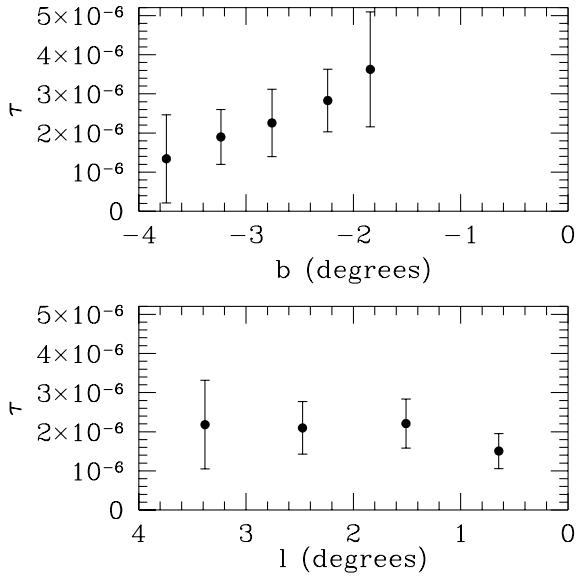

Fig. 14.— Average optical depth in latitude and longitude strips for events within 5.5° from the Galactic center. Gradient in b is much steeper than the one in l.

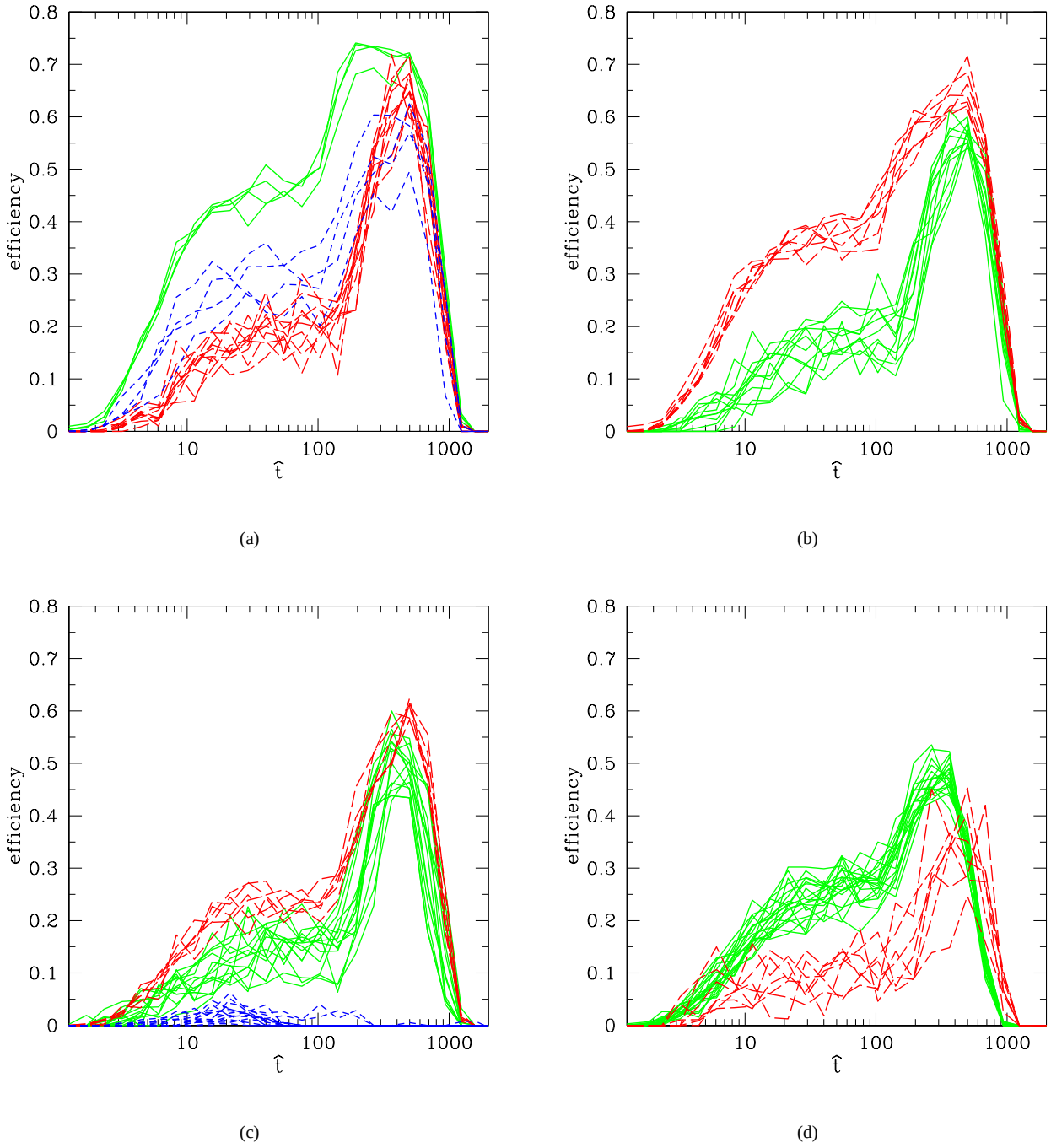

Fig. 12.— Clump detection efficiencies versus $\hat{t}$ for all fields. **(a)** solid green - 108, 113, 118, 119; red long dashed - 116, 124, 125, 136, 142, 143, 146, 148, 149, 155; blue short dashed - 110, 159, 161, 162 **(b)** solid green - 111, 122, 131, 132, 137, 150, 152, 158, 163, 171, 174; red dashed - 101, 104, 105, 109, 114, 120, 128 **(c)** solid green - 127, 133, 138, 144, 147, 151, 153, 154, 156, 157, 160, 166, 168; red long dashed - 102, 103, 115, 121, 167; blue short dashed - 106, 107, 112, 117, 123, 126, 129, 130, 135, 141, 164, 165, 169, 170 **(d)** solid green - 176-180, 301-311, 401-403; red dashed - 134, 139, 140, 145, 172, 173, 175. Note that fields 176-180 and fields 401-403 efficiencies are low because they were not observed for the whole 7 year period. As explained earlier, fields 300-311 are not included in the analysis but are included here for completeness.

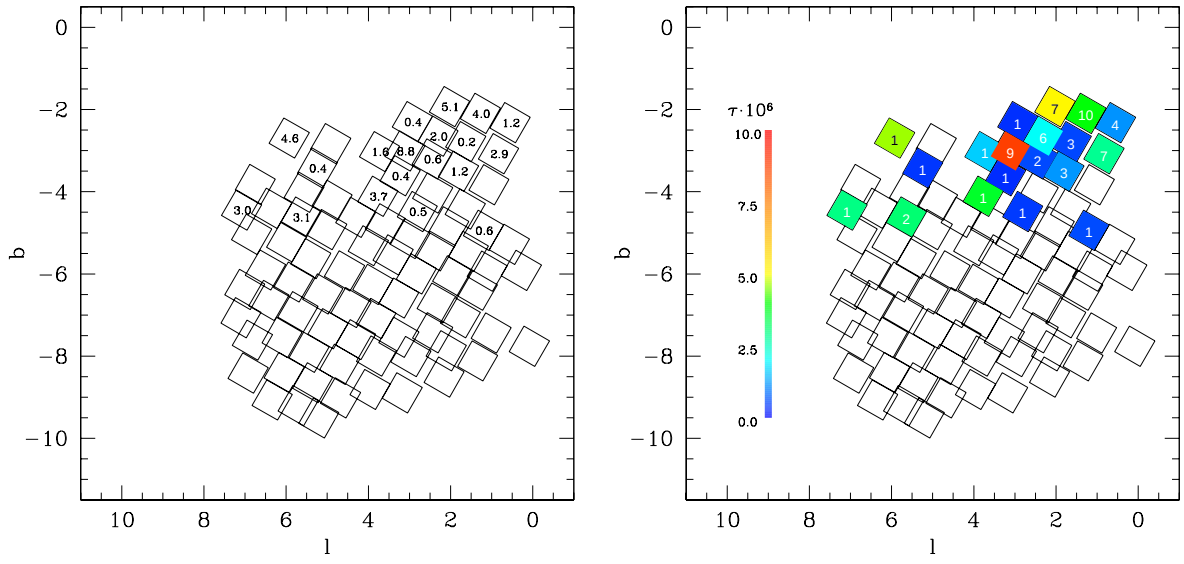

(a) (b)

Fig. 13.— (a) Microlensing optical depth ($\times 10^6$) toward each field that contains a clump event. (b) Optical depth in each field with a detected clump event and the number of events in that field. Only analyzed fields are shown in both panels.

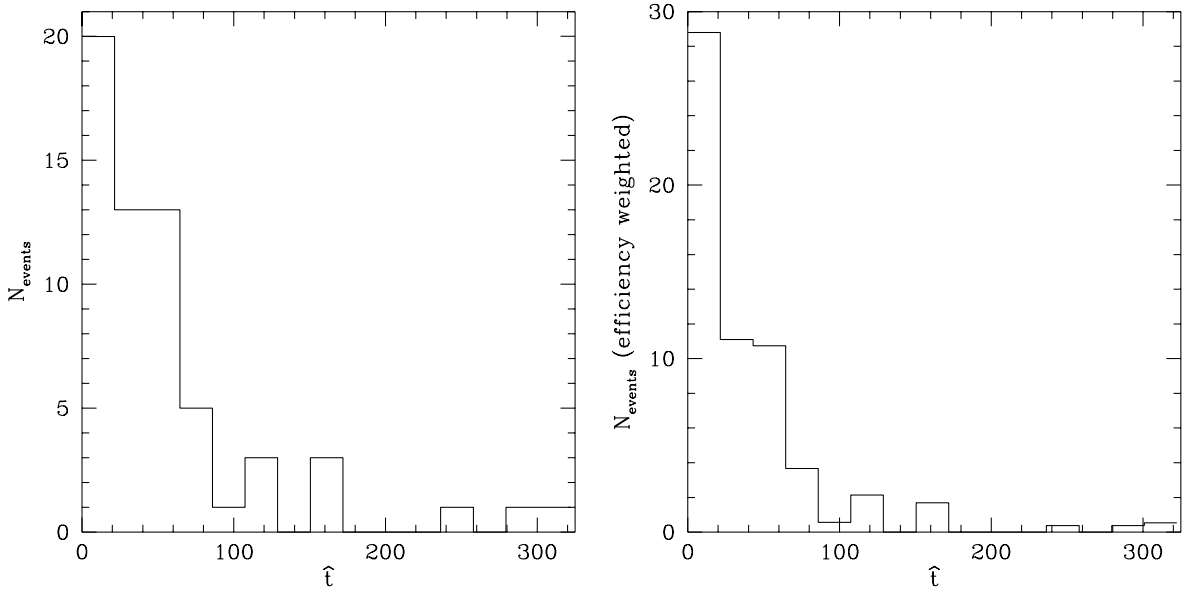

Fig. 15.— Left panel shows the histogram of the distribution of Einstein crossing times. The right panel shows the same distribution with each event weighted by its inverse efficiency and renormalized.

A. Optical depth estimation

The optical depth is usually defined as the probability of a microlensing event happening at a given time on any given star. An "event" is usually defined as occurring when a lens comes within one Einstein radius of the line-of-sight to the source. This is easily determined observationally since the formula for magnification is

$$A(u) = \frac{u^2+2}{u(u^2+4)^{1/2}}, \tag{A1}$$

where $u = l/R_E$ is the distance of the lens from the line-of-sight in units of the Einstein radius R_E, and

$$R_E = 2\left(\frac{GMD_l(D_s-D_l)}{c^2 D_s}\right)^{1/2}, \tag{A2}$$

where M is the mass of the lens, D_s is the observer-source distance, and D_l is the observer-lens distance. Thus $u \leq 1$ or $A \geq 1.34$ means the line-of-sight is within one Einstein radius.

To estimate the probability of lensing occurring we must use the observed microlensing events. First consider the case of a 100% efficient microlensing experiment. When there are many stars observed, one would like to find the probability of lensing per star at a given time by dividing the number of stars being lensed at a given time by the total number of observed stars. Observationally, however, one cannot tell whether or not a given star is being lensed; one only measures stars brightening and then fading as the line-of-sight enters and leaves the Einstein radius. In this case one can estimate the lensing probability by the fraction of the total available observing time that a given star spends lensed with $A \geq 1.34$. With many stars, the optical depth is thus estimated as $\tau = \sum_i t_i/E$, where t_i is the time inside the Einstein radius (i.e. $A > 1.34$), and the exposure $E = N_* T_{\rm obs}$ is the number of observed stars times the duration of the observations. The quantity t_i is easily found from the two microlensing fit parameters: $\hat{t}_i$, the Einstein diameter crossing time, and $A_{{\rm max},i}$, the maximum magnification:

$$t_i = \hat{t}_i\sqrt{1-u_{{\rm min},i}^2}, \tag{A3}$$

where $u_{\rm min,i}$ is found from $A_{{\rm max},i}$ by inverting equation (A1) above.

For an imperfect observational program only a fraction ϵ of microlensing events will be detected. Calculating this efficiency as a function of event duration and magnification allows a correction to be made for each detected event giving the formula we use:

$$\tau = \frac{1}{E}\sum_{i=1}^{N_{\rm events}} \frac{t_i}{\epsilon(t_i, A_{{\rm max},i})}. \tag{A4}$$

If one wished to use the fit $\hat{t}_i$ and avoid using t_i one could replace t_i in the formula above with an estimate of the typical value of $\hat{t}$. This could be done by noting that every impact parameter, u, between 0 and 1 is equally likely (given perfect efficiency) and so averaging over all impact parameters for a given Einstein ring gives $\langle t_i\rangle = \frac{\pi}{4}\langle \hat{t}_i\rangle$. Since for a large number of events the sum over t_i is effectively an average over t_i, one could replace t_i with $\frac{\pi}{4}\hat{t}_i$ inside the sum. The resulting formula is equation (12), and has been used in the past.

One difference between the two formulas is that the new formula allows weighting each event with an efficiency calculated as a function of both $\hat{t}_i$ and $u_{{\rm min},i}$. When using the sum over $\hat{t}_i$ one usually weights by the efficiency only as a function of $\hat{t}$.

There is one subtlety when calculating efficiencies for each event, rather than as a function of $\hat{t}$. Since we used a cut $A_{\rm max} \geq 1.5$ and optical depth is defined as the probability of finding events with $A_{\rm max} \geq 1.34$, the above formula needs to be multiplied by a correction factor of 1.09 to account for events with $1.34 \leq A_{\rm max} < 1.5$. These low amplification events are not detected so can not be included in the efficiency calculation which only inputs simulated events for the measured values of t and $A_{\rm max}$. When efficiencies are calculated as a function of $\hat{t}$, events with such values are input, but not detected, resulting in a lower efficiency (and therefore higher optical depth) for that value of $\hat{t}$. One can invert equation (A1) and find that $u(1.5) = 0.83$, and $u(1.34) = 1$. With the assumption that the lens is

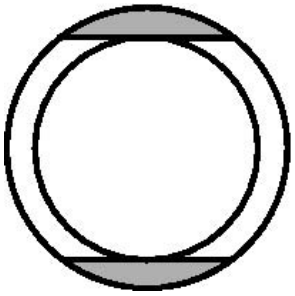

Fig. 16.— Area of Einstein rings used for calculating optical depths, shaded regions are missed by our cuts.

moving at uniform velocity through the line of sight, the correction factor becomes simply the ratio of area within the Einstein ring to the area in the ring with an impact parameter less than 0.83. In Figure 16 one can see the Einstein ring and the ring at $u = 0.83$ ($A_{\rm max} = 1.5$). The areas missed with our cuts are the small sections on the top and bottom of the circle.

B. Upper limits on optical depth

Optical depth in a given field can be estimated as a number of events in a given field multiplied by the contribution of a typical event. Therefore, one can define upper limits on the optical depth in fields with no events as:

$$\tau_f^{\rm lim,CL} = \nu^{\rm CL} \tau_f^{1\,\rm event}, \tag{B1}$$

where $\tau_f^{1\,\rm event}$ would be a typical contribution of one event to the optical depth in field f and $\nu^{\rm CL}$ is a multiplication factor dependent on the confidence level (CL). Equation (B1) can be expressed as:

$$\tau_f^{\rm lim,CL} = \nu^{\rm CL} \frac{\pi}{4 N_f T_{\rm obs}} \left\langle \frac{\hat{t}}{\epsilon(\hat{t})} \right\rangle_f , \tag{B2}$$

where the angle brackets indicate an average in field f. Let us first note that for each field, we have efficiencies $\epsilon(\hat{t})$, which come from our simulations. However, since we have no events in the fields of interest we cannot estimate the right side of equation (B2) based exclusively on the data in field f. Therefore, we are forced to assume that duration distribution in the entire area of our bulge survey is universal and proceed as follows. Based on the observed duration distribution in fields with events and efficiencies in those fields we can recover the intrinsic duration distribution of events. This distribution can then be mapped using the efficiencies in field f to recover the hypothetical duration distribution that would be observed in field f. Each $\hat{t}_i$ from our clump sample contributes to the hypothetical distribution in field f with a weight $w_{f,i} \equiv \epsilon_f(\hat{t}_i)/\epsilon_i(\hat{t}_i)$, where ϵ_f is the efficiency in field f, and ϵ_i is the efficiency in the event's field of origin. We now may express:

$$\begin{aligned} \left\langle \frac{\hat{t}}{\epsilon(\hat{t})} \right\rangle_f &= \frac{\sum_{i=1}^{N_{\rm events}} w_{f,i} \left(\hat{t}_i / \epsilon_f(\hat{t}_i) \right)}{\sum_{i=1}^{N_{\rm events}} w_{f,i}} \\ &= \frac{\sum_{i=1}^{N_{\rm events}} \hat{t}_i / \epsilon_i(\hat{t}_i)}{\sum_{i=1}^{N_{\rm events}} \epsilon_f(\hat{t}_i)/\epsilon_i(\hat{t}_i)} \end{aligned} \tag{B3}$$

Substitution of equation (B3) to equation (B2) leads to:

$$\tau_f^{\rm lim,CL} = \nu^{\rm CL} \frac{\pi}{4 N_f T_{\rm obs}} \frac{\sum_{i=1}^{N_{\rm events}} \hat{t}_i / \epsilon_i(\hat{t}_i)}{\sum_{i=1}^{N_{\rm events}} \epsilon_f(\hat{t}_i)/\epsilon_i(\hat{t}_i)}, \tag{B4}$$

which is the formula that we use in §5. Let us explain the role of the multiplication factor $\nu^{\rm CL}$. The number of observed events is Poisson distributed. To constrain optical depth we simply ask what is the upper limit on the number of expected events given 0 detected events for the Poisson distribution. We can obtain the necessary number of expected events $\nu^{\rm CL}$ that rules out $\tau_f^{\rm lim,CL}$ or larger at CL from the following equation:

$$\exp(-\nu^{\rm CL}) = \frac{1.0 - {\rm CL}}{2} \tag{B5}$$

For 1σ (68.17%) CL, one obtains $\nu^{1\sigma} = 1.8379$.

REFERENCES

Afonso, C., et al. 2003, A&A, 404, 145

Alcock, C., et al. 1997a, ApJ, 479, 119

Alcock, C., et al. 1997b, ApJ, 486, 697

Alcock, C., et al. 1998, ApJ, 494, 396

Alcock, C., et al. 1999, PASP, 111, 1539

Alcock, C., et al. 2000a, ApJ, 541, 734

Alcock, C., et al. 2000b, ApJ, 542, 281

Alcock, C., et al. 2000c, ApJ, 541, 270

Binney, J., Bissantz, N., & Gerhard, O. 2000, ApJ, 537, L99

Bissantz N., Englmaier P., Binnet J., & Gerhard O. 1997, MNRAS, 289, 651

CERN Lib., 2003, http://wwwasdoc.web.cern.ch/wwwasdoc/minuit/minmain.html

Evans N.W., & Belokurov V. 2002, ApJ, 567, L119

Gould, A., Popowski, P., & Terndrup, D.T. 1998, ApJ, 492, 778

Griest, K. et al. 1991, ApJ, 372, L79

Gyuk, G. 1999, ApJ, 510, 205

Han, C, & Gould, A. 1995, ApJ, 449, 521

Han, C, & Gould, A. 1996, ApJ, 467, 540

Han, C, & Gould, A. 2003, ApJ, 592, 172

Hart, J., et al. 1996, PASP, 108, 220

Kiraga, M., & Paczyński, B. 1994, ApJ, 430, L101

Marshall, S.L., et al. 1994, in IAU Symp. 161, Astronomy From Wide Field Imaging, ed. H.T. MacGillivray, et al., (Dordrecht: Kluwer)

Metcalf, R.B. 1995, AJ, 110, 869

Nair V., & Miralda-Escudé, J. 1999, ApJ, 515, 206

Paczyński, B. 1991, ApJ, 371, L63

Popowski, P. 2000, ApJ, 528, L9

Popowski, P. 2002, preprint (astro-ph/0205044)

Popowski, P., et al. 2001a, ASP Conference Series: 'Microlensing 2000: A New Era of Microlensing Astrophysics', eds. J.W. Menzies & P.D. Sackett, Vol. 239, p. 244 (astro-ph/0005466)

Popowski, P., et al. 2001b, ASP Conference Series: 'Astrophysical Ages and Times Scales', eds. T. von Hippel, C. Simpson, and N. Manset., Vol. 245, p. 358 (astro-ph/0202502)

Popowski, P., et al. 2003a, invited review, to appear in 'Gravitational Lensing: A Unique Tool For Cosmology', Aussois 2003, eds. D. Valls-Gabaud & J.-P. Kneib (astro-ph/0304464)

Popowski, P., Cook, K.H., & Becker, A.C. 2003b, AJ, 126, 2910

Sevenster, M.N., & Kalnajs, A.J. 2001, AJ, 122, 885

Stanek, K.Z. 1996, ApJ, 460, L37

Stubbs, C.W., et al. 1993, in Proceedings of the SPIE, Charge Coupled Devices and Solid State Optical Sensors III, ed. M. Blouke, 1900, 192

Sumi, T., et al. 2003, ApJ, 591, 204

Sumi, T. 2004, MNRAS, 349, 193

Thomas, C.L., et al. 2004 (companion paper)

Udalski, A., et al. 1993, Acta Astron. 43, 69

Udalski, A., et al. 1994a, ApJ, 426, L69

Udalski, A., et al. 1994b, Acta Astron., 44, 165

Udalski, A. 2003, ApJ, 590, 284

Woźniak, P., & Paczyński, B. 1997, ApJ, 487, 55

Zhao, H., & Mao, S. 1996, MNRAS, 283, 1197

Zhao, H., Spergel, D.N.,& Rich, R.M. 1995, ApJ, 440, L13

This 2-column preprint was prepared with the AAS LaTeX macros v5.0.

TABLE 1
SELECTION CRITERIA

Selection	Description
microlensing fit parameter cuts:	
$N_{(V-R)} > 0$	require color information
$\chi^2_{out} < 3.0,\ \chi^2_{out} > 0.0$	require high quality baselines
$N_{amp} \geq 8$	require 8 points in the amplified region
$N_{rising} \geq 1,\ N_{falling} \geq 1$	require at least one point in the rising and falling part of the peak
$A_{max} > 1.5$	magnification threshold
$(A_{max} - 1) > 2.0(\sigma_R + \sigma_B)$	signal to noise cut on amplification
$(\sigma_R + \sigma_B) < (0.05\,\delta\chi^2)/(N_{amp}\,\chi^2_{in}\,\chi^2_{out})$	remove spurious photometric signals caused by nearby saturated stars
$(N_{amp}\,\chi^2_{out}\,f_{chrom})/(\mathit{befaft}\,\delta\chi^2) < 0.0003$	remove spurious photometric signals caused by nearby saturated stars
$(N_{amp}\,\chi^2_{in})/(\mathit{befaft}\,\delta\chi^2) < 0.00004$	remove spurious photometric signals caused by nearby saturated stars
$\delta\chi^2/fc2 > 320.0$	good overall fit to microlensing lc shape
$\delta\chi^2/\chi^2_{peak} \geq 400.0$	same quality fit in peak as whole lc
$0.5(rcrda + bcrda) \leq 143.0$	source star not too crowded
$\xi^{auto}_B/\xi^{auto}_R < 2.0$	remove long period variables
$t_0 > 419.0,\ t_0 < 2850.0$	constrain the peak to period of observations
$\hat{t} < 1700$	limit event duration to ∼half the span of observations
clump giant cuts:	
$V \geq 15,\ V \leq 20.5$	select bright stars with reliabale photometry
$V \geq 4.2(V-R) + 12.4$	define bright boundary of extinction strip
$V \leq 4.2(V-R) + 14.2$	define faint boundry of extinction strip
$(V-R) \geq (V-R)_{boundary}$	avoid main sequence contamination
exclude fields $300 - 311$	avoid disk contamination

NOTE.—Designations V and $(V-R)$ indicate baseline quantities, i.e. the ones in the limit of no microlensing-induced amplification.

TABLE 2

EVENT PARAMETERS

field.tile.seq	RA (J2000)	DEC (J2000)	l	b	V	$(V-R)$	$(V-R)_{\rm boundary}$	t_0	$\hat{t}$	$A_{\rm max}$	$\frac{\chi^2}{n_{dof}}$
101.21689.315	18 06 58.32	−27 27 45.7	3.639	−3.327	17.50	1.09	0.81	593.5	165	4.80	1.19
102.22466.140	18 08 47.04	−27 40 47.3	3.643	−3.783	16.81	0.95	0.81	1275.6	153	3.88	0.95
104.19992.858	18 02 53.76	−27 57 50.0	2.761	−2.784	18.59	1.09	0.85	1169.7	106	2.23	2.15
104.20119.6312[a]	18 03 20.64	−28 08 14.6	2.658	−2.955	17.99	1.06	0.78	1975.3	38.7	1.62	1.62
104.20251.50	18 03 34.08	−28 00 19.1	2.797	−2.933	17.33	0.93	0.82	493.9	287	10.1	1.75
104.20251.1117	18 03 29.04	−28 00 31.0	2.785	−2.919	18.22	0.98	0.82	463.2	45.5	2.09	0.93
104.20259.572	18 03 33.36	−27 27 47.2	3.269	−2.665	18.16	1.19	0.91	538.5	14.2	1.58	1.56
104.20382.803	18 03 53.28	−27 57 35.6	2.872	−2.973	17.79	0.96	0.84	1765.8	254	5.72	4.40
104.20515.498	18 04 09.60	−27 44 35.2	3.090	−2.919	17.63	0.99	0.81	2061.7	53.6	1.76	1.42
104.20640.8423[b]	18 04 33.60	−28 07 31.8	2.800	−3.183	17.15	0.98	0.79	2374.9	30.8	1.65	2.23
104.20645.3129	18 04 26.16	−27 47 35.2	3.077	−2.997	17.68	1.07	0.83	1558.3	152	1.82	0.77
105.21813.2516	18 07 06.96	−27 52 34.3	3.292	−3.555	17.41	1.08	0.83	1928.5	17.5	13.2	1.14
108.18947.3618	18 00 29.04	−28 19 20.3	2.186	−2.498	17.72	1.10	0.89	1287.9	45.6	2.05	0.94
108.18951.593[‡]	18 00 33.84	−28 01 10.6	2.458	−2.363	18.07	1.18	0.95	1991.6	47.3	4.05	7.02
108.18951.1221	18 00 25.92	−28 02 35.2	2.423	−2.350	18.94	1.18	0.95	583.6	45.8	2.16	0.92
108.18952.941	18 00 36.00	−27 58 30.0	2.501	−2.348	18.90	1.16	1.02	1324.9	66.9	2.39	1.11
108.19074.550	18 00 52.32	−28 29 52.1	2.076	−2.659	17.54	1.03	0.88	2050.6	9.30	1.78	0.97
108.19334.1583	18 01 26.40	−28 31 14.2	2.117	−2.779	17.67	0.94	0.86	1231.4	18.5	4.09	0.38
109.20119.1051[a]	18 03 20.64	−28 08 14.6	2.658	−2.955	18.09	0.97	0.78	1977.6	28.7	1.62	1.01
109.20640.360[b]	18 04 33.60	−28 07 32.5	2.799	−3.183	17.33	1.05	0.79	2375.1	28.7	1.67	0.72
110.22455.842	18 08 51.36	−28 27 11.2	2.971	−4.169	18.28	0.98	0.76	1900.1	19.8	2.54	0.84
113.18552.581	17 59 36.00	−28 36 24.1	1.842	−2.470	17.60	1.02	0.86	603.7	27.9	1.77	1.11
113.18804.1061	18 00 03.36	−29 11 04.2	1.390	−2.843	18.28	1.00	0.84	1166.6	6.50	1.62	0.96
113.19192.365	18 01 06.96	−29 18 53.6	1.391	−3.109	17.80	1.17	0.96	2092.6	36.9	1.97	0.52
114.19712.813	18 02 11.52	−29 19 20.6	1.500	−3.317	18.12	1.08	0.87	1643.4	23.7	3.58	0.62
114.19846.777	18 02 36.72	−29 01 41.9	1.801	−3.252	17.98	1.02	0.80	545.4	65.0	1.55	1.86
114.19970.843	18 02 54.48	−29 26 29.4	1.472	−3.511	17.99	0.96	0.85	1281.9	14.7	4.47	0.65
118.18014.320	17 58 25.20	−29 47 59.6	0.678	−2.840	17.01	0.97	0.89	877.6	25.5	1.58	1.05
118.18141.731[‡]	17 58 36.72	−30 02 19.3	0.491	−2.995	17.92	1.06	0.94	884.1	9.80	12.6	0.65
118.18271.738	17 58 52.56	−30 02 08.2	0.522	−3.043	18.25	1.18	0.96	456.4	53.7	2.23	0.69
118.18402.495	17 59 13.92	−29 55 53.4	0.651	−3.058	17.63	1.08	0.93	454.1	23.8	3.60	0.96
118.18797.1397	18 00 06.96	−29 38 06.0	1.004	−3.078	19.34	1.30	0.97	2013.1	126	8.35	1.07
118.19182.891	18 01 09.84	−29 56 19.0	0.852	−3.425	17.97	0.93	0.84	2367.0	13.6	6.28	1.20
118.19184.939	18 01 10.32	−29 48 55.4	0.960	−3.366	18.07	0.99	0.83	2692.8	74.4	2.14	1.13
121.22032.133	18 07 46.80	−30 39 41.4	0.915	−5.025	16.37	0.86	0.75	1287.3	19.5	1.58	2.51

TABLE 2—*Continued*

field.tile.seq	RA (J2000)	DEC (J2000)	l	b	V	$(V-R)$	$(V-R)_{\rm boundary}$	t_0	$\hat{t}$	$A_{\rm max}$	$\frac{\chi^2}{n_{dof}}$
158.27444.129	18 20 10.32	−25 08 25.8	7.097	−4.827	16.97	0.76	0.63	2376.4	41.7	2.31	1.80
162.25865.442	18 16 30.72	−26 26 58.2	5.549	−4.712	17.52	0.90	0.73	1225.3	60.9	1.58	1.32
162.25868.405	18 16 46.08	−26 11 43.1	5.801	−4.643	17.33	0.83	0.77	1222.8	30.8	2.77	1.39
176.18826.909	18 00 15.36	−27 42 47.9	2.691	−2.153	18.77	1.20	1.01	2364.7	24.3	1.77	1.17
178.23531.931	18 11 17.52	−25 59 51.4	5.391	−3.467	18.71	1.10	0.92	1590.3	13.7	2.18	1.08
180.22240.202	18 07 57.84	−25 24 48.2	5.542	−2.528	18.92	1.40	0.98	1286.9	311	3.42	1.15
401.47991.1840	17 57 07.44	−28 13 44.0	1.899	−1.810	19.46	1.37	1.12	1953.0	44.7	1.92	0.61
401.47994.1182	17 57 07.92	−28 00 27.7	2.091	−1.701	19.65	1.53	1.23	2362.7	60.6	3.68	1.05
401.48052.861	17 57 23.76	−28 10 24.6	1.977	−1.834	18.75	1.31	1.13	2291.5	72.0	2.65	0.69
401.48167.1934	17 57 57.36	−28 27 09.7	1.796	−2.080	18.42	1.23	1.09	2179.0	125	2.53	0.89
401.48229.760‡	17 58 13.44	−28 20 32.3	1.921	−2.076	18.07	1.15	1.00	2694.5	20.1	1.82	1.18
401.48408.649‡	17 59 08.88	−28 24 54.7	1.959	−2.289	17.70	1.20	0.92	2325.4	74.6	3.07	1.30
401.48469.789	17 59 22.32	−28 20 21.8	2.050	−2.294	18.23	1.17	0.92	1554.8	5.70	5.96	0.42
402.47678.1666	17 55 22.56	−29 04 12.7	0.978	−1.901	19.19	1.31	1.07	2393.1	13.6	2.48	0.88
402.47737.1590	17 55 41.52	−29 09 00.7	0.944	−2.001	18.49	1.04	0.99	1552.3	5.50	2.79	1.03
402.47742.3318	17 55 42.96	−28 49 17.4	1.230	−1.840	20.19	1.62	1.10	1377.1	50.1	8.64	1.21
402.47796.1893	17 56 10.80	−29 10 44.4	0.972	−2.107	19.52	1.33	1.03	1678.7	19.3	22.5	1.47
402.47798.1259	17 56 11.04	−29 06 14.0	1.038	−2.070	19.72	1.36	1.10	1583.7	47.6	4.94	1.38
402.47799.1736	17 56 07.20	−28 58 32.5	1.142	−1.994	19.59	1.29	1.16	2410.0	115	2.26	0.47
402.47856.561	17 56 24.96	−29 12 56.5	0.966	−2.170	18.81	1.38	1.15	1566.6	12.3	2.14	1.63
402.47862.1576‡	17 56 20.64	−28 47 42.0	1.323	−1.945	19.47	1.30	1.15	2028.5	54.3	7.52	6.13
402.48158.1296	17 57 47.52	−29 03 54.4	1.247	−2.346	18.69	1.12	1.01	2325.7	15.9	3.94	0.98
402.48280.502‡	17 58 24.96	−28 57 46.4	1.404	−2.422	18.17	1.18	0.90	1342.5	25.5	2.08	1.14
403.47491.770	17 54 38.64	−29 33 13.0	0.480	−2.007	17.94	1.29	1.04	2633.9	48.5	2.43	0.99
403.47550.807	17 55 00.00	−29 35 03.8	0.492	−2.089	17.95	1.21	1.04	2774.3	11.6	3.60	0.87
403.47610.576	17 55 17.04	−29 37 40.8	0.486	−2.164	17.54	1.13	0.98	2657.9	9.60	4.75	2.56
403.47845.495	17 56 22.80	−29 55 16.3	0.351	−2.517	18.20	1.24	1.07	1945.8	15.0	2.03	0.88

NOTE.—Designations:
‡: binary event,
[a] and [b]: each superscript marks two members of a pair that represents a single microlensing event in two overlapping fields.

TABLE 3
OPTICAL DEPTH CONTRIBUTION BY EVENT

field.tile.seq	t_i	$\hat{t}$	$A_{\max,i}$	$\epsilon(t_i, A_{\max,i})$	$\epsilon(\hat{t})$	$\tau(t_i)$	$\tau(\hat{t})$
101.21689.315	161	165	4.80	0.68	0.55	1.62	1.47
102.22466.140	147	153	3.88	0.39	0.32	3.67	3.34
104.19992.858	93.4	107	2.23	0.55	0.43	1.12	1.19
104.20119.6312	25.7	38.3	1.62	0.48	0.38	0.36	0.47
104.20251.50	285	287	10.1	0.77	0.63	2.44	2.18
104.20251.1117	38.7	45.6	2.09	0.46	0.39	0.56	0.56
104.20259.572	9.22	14.2	1.58	0.41	0.33	0.15	0.20
104.20382.803	250	254	5.73	0.78	0.62	2.11	1.95
104.20515.498	40.4	53.5	1.76	0.48	0.39	0.56	0.65
104.20640.8423	21.4	30.8	1.65	0.47	0.4	0.30	0.37
104.20645.3129	118	152	1.82	0.66	0.52	1.19	1.38
105.21813.2516	17.5	17.5	13.2	0.40	0.31	0.35	0.32
108.18947.3618	38.4	45.6	2.05	0.56	0.48	0.38	0.38
108.18951.593	45.8	47.3	4.05	0.57	0.47	0.44	0.39
108.18951.1221	39.5	45.8	2.16	0.57	0.48	0.38	0.38
108.18952.941	59.7	66.9	2.39	0.58	0.46	0.56	0.57
108.19074.550	7.07	9.26	1.78	0.41	0.34	0.09	0.11
108.19334.1583	17.9	18.5	4.09	0.53	0.42	0.18	0.17
109.20119.1051	19.4	28.7	1.62	0.44	0.4	0.29	0.34
109.20640.360	20.4	28.7	1.67	0.45	0.4	0.29	0.34
110.22455.842	18.0	19.8	2.54	0.41	0.33	0.46	0.46
113.18552.581	21.2	27.9	1.77	0.53	0.46	0.21	0.23
113.18804.1061	4.44	6.53	1.62	0.29	0.27	0.08	0.09
113.19192.365	30.4	36.9	1.97	0.59	0.49	0.27	0.28
114.19712.813	22.7	23.7	3.57	0.44	0.36	0.36	0.33
114.19846.777	40.0	64.9	1.55	0.46	0.39	0.61	0.84
114.19970.843	14.3	14.7	4.47	0.45	0.32	0.22	0.23
118.18014.320	16.3	25.5	1.58	0.54	0.44	0.18	0.24
118.18141.731	9.74	9.77	12.6	0.45	0.34	0.12	0.12
118.18271.738	46.9	53.7	2.23	0.56	0.46	0.49	0.49
118.18402.495	22.8	23.8	3.60	0.54	0.43	0.24	0.23
118.18797.1397	125	126	8.35	0.73	0.58	1.00	0.91
118.19182.891	13.4	13.6	6.28	0.49	0.39	0.16	0.15
118.19184.939	64.0	74.4	2.14	0.56	0.48	0.66	0.65
121.22032.133	12.5	19.4	1.58	0.27	0.21	0.59	0.85
158.27444.129	36.8	41.7	2.31	0.22	0.2	2.96	2.59
162.25865.442	39.5	60.9	1.58	0.33	0.24	1.73	2.63
162.25868.405	28.5	30.8	2.77	0.30	0.24	1.38	1.33
176.18826.909	18.4	24.3	1.77	0.26	0.24	0.37	0.39
178.23531.931	11.9	13.7	2.18	0.25	0.19	0.43	0.46
180.22240.202	297	312	3.42	0.58	0.44	4.62	4.62
401.47991.1840	36.2	44.7	1.92	0.29	0.24	0.55	0.60
401.47994.1182	58.2	60.6	3.68	0.31	0.25	0.83	0.78
401.48052.861	66.0	72.0	2.65	0.34	0.25	0.88	0.93
401.48167.1934	113	125	2.54	0.38	0.33	1.34	1.23

TABLE 3—*Continued*

field.tile.seq	t_i	$\hat{t}$	$A_{\max,i}$	$\epsilon(t_i, A_{\max,i})$	$\epsilon(\hat{t})$	$\tau(t_i)$	$\tau(\hat{t})$
401.48229.760	15.7	20.1	1.82	0.24	0.20	0.29	0.33
401.48408.649	70.1	74.6	3.07	0.32	0.25	0.98	0.96
401.48469.789	5.59	5.67	6.01	0.098	0.059	0.25	0.31
402.47678.1666	12.3	13.7	2.48	0.26	0.20	0.17	0.18
402.47737.1590	5.06	5.46	2.8	0.13	0.086	0.15	0.17
402.47742.3318	49.8	50.1	8.64	0.32	0.26	0.59	0.52
402.47796.1893	19.3	19.3	22.7	0.29	0.24	0.25	0.22
402.47798.1259	46.6	47.6	4.95	0.31	0.26	0.56	0.49
402.47799.1736	101	115	2.26	0.38	0.32	0.99	0.98
402.47856.561	10.5	12.3	2.14	0.24	0.20	0.16	0.17
402.47862.1576	53.8	54.3	7.52	0.34	0.26	0.6	0.55
402.48158.1296	15.4	15.9	3.94	0.29	0.21	0.20	0.21
402.48280.502	21.7	25.5	2.08	0.3	0.24	0.27	0.28
403.47491.770	43.5	48.5	2.43	0.31	0.26	0.57	0.53
403.47550.807	11.1	11.6	3.60	0.21	0.16	0.20	0.20
403.47610.576	9.37	9.59	4.76	0.2	0.14	0.19	0.19
403.47845.495	12.6	15.0	2.03	0.25	0.20	0.20	0.22

TABLE 4

ALTERNATIVE DESIGNATIONS OF OUR EVENTS

field.tile.seq	RA (J2000)	DEC (J2000)	MACHO Alert	EROS	OGLE
101.21689.315	18 06 58.32	−27 27 45.7	101-B		
102.22466.140	18 08 47.04	−27 40 47.3	95-BLG-13		
104.19992.858	18 02 53.76	−27 57 50.0			
104.20119.6312	18 03 20.64	−28 08 14.6	97-BLG-34		
104.20251.50	18 03 34.08	−28 00 19.1	104-C		
104.20251.1117	18 03 29.04	−28 00 31.0	104-D		
104.20259.572	18 03 33.36	−27 27 47.2	104-A		
104.20382.803	18 03 53.28	−27 57 35.6	96-BLG-12	#16, BLG-12	
104.20515.498	18 04 09.60	−27 44 35.2	97-BLG-58	#11, BLG-11	BUL_SC35-144974
104.20640.8423	18 04 33.60	−28 07 31.8		#7, BLG-13	1998-BUL-23
104.20645.3129	18 04 26.16	−27 47 35.2	96-BLG-1		
105.21813.2516	18 07 06.96	−27 52 34.3	97-BLG-10		
108.18947.3618	18 00 29.04	−28 19 20.3			
108.18951.593	18 00 33.84	−28 01 10.6	97-BLG-28		
108.18951.1221	18 00 25.92	−28 02 35.2	108-A		
108.18952.941	18 00 36.00	−27 58 30.0	95-BLG-32		
108.19074.550	18 00 52.32	−28 29 52.1	97-BLG-59		
108.19334.1583	18 01 26.40	−28 31 14.2	95-BLG-14		
109.20119.1051	18 03 20.64	−28 08 14.6			
109.20640.360	18 04 33.60	−28 07 32.5		#7, BLG-13	1998-BUL-23
110.22455.842	18 08 51.36	−28 27 11.2	97-BLG-5	#4, BLG-28	
113.18552.581	17 59 36.00	−28 36 24.1	113-A		
113.18804.1061	18 00 03.36	−29 11 04.2	95-BLG-4		
113.19192.365	18 01 06.96	−29 18 53.6			
114.19712.813	18 02 11.52	−29 19 20.6	96-BLG-19		
114.19846.777	18 02 36.72	−29 01 41.9	114-A		
114.19970.843	18 02 54.48	−29 26 29.4	95-BLG-24		
118.18014.320	17 58 25.20	−29 47 59.6	94-BLG-3		
118.18141.731	17 58 36.72	−30 02 19.3	94-BLG-4		
118.18271.738	17 58 52.56	−30 02 08.2	118-D		
118.18402.495	17 59 13.92	−29 55 53.4	118-C		
118.18797.1397	18 00 06.96	−29 38 06.0	97-BLG-26	#14, BLG-4	
118.19182.891	18 01 09.84	−29 56 19.0	98-BLG-33		1998-BUL-22
118.19184.939	18 01 10.32	−29 48 55.4	99-BLG-12	#12, BLG-5	1999-BUL-07
121.22032.133	18 07 46.80	−30 39 41.4			
158.27444.129	18 20 10.32	−25 08 25.8			
162.25865.442	18 16 30.72	−26 26 58.2			
162.25868.405	18 16 46.08	−26 11 43.1	95-BLG-8		
176.18826.909	18 00 15.36	−27 42 47.9			
178.23531.931	18 11 17.52	−25 59 51.4	178-A		
180.22240.202	18 07 57.84	−25 24 48.2			
401.47991.1840	17 57 07.44	−28 13 44.0	97-BLG-19		
401.47994.1182	17 57 07.92	−28 00 27.7	98-BLG-26		
401.48052.861	17 57 23.76	−28 10 24.6	98-BLG-10		
401.48167.1934	17 57 57.36	−28 27 09.7			
401.48229.760	17 58 13.44	−28 20 32.3	99-BLG-25		
401.48408.649	17 59 08.88	−28 24 54.7	98-BLG-14		BUL_SC20-395103
401.48469.789	17 59 22.32	−28 20 21.8			
402.47678.1666	17 55 22.56	−29 04 12.7	98-BLG-39		

TABLE 4—*Continued*

field.tile.seq	RA (J2000)	DEC (J2000)	MACHO Alert	EROS	OGLE
402.47737.1590	17 55 41.52	−29 09 00.7			
402.47742.3318	17 55 42.96	−28 49 17.4			
402.47796.1893	17 56 10.80	−29 10 44.4	402-B		
402.47798.1259	17 56 11.04	−29 06 14.0			
402.47799.1736	17 56 07.20	−28 58 32.5	98-BLG-37		
402.47856.561	17 56 24.96	−29 12 56.5			
402.47862.1576	17 56 20.64	−28 47 42.0	97-BLG-41		
402.48158.1296	17 57 47.52	−29 03 54.4	98-BLG-19		1998-BUL-17
402.48280.502	17 58 24.96	−28 57 46.4			
403.47491.770	17 54 38.64	−29 33 13.0	99-BLG-7		1999-BUL-02
403.47550.807	17 55 00.00	−29 35 03.8	99-BLG-54		1999-BUL-41
403.47610.576	17 55 17.04	−29 37 40.8			
403.47845.495	17 56 22.80	−29 55 16.3	97-BLG-17		

TABLE 5
EVENTS WITH LIGHT CURVE DEVIATIONS

field.tile.seq	Comments
101.21689.315	possible parallax
104.20119.6312/109.20119.1051	parallax or xallarap
104.20251.50	parallax
104.20382.803	parallax
104.20640.8423	—
105.21813.2516	possible red blend
108.18951.593	binary
114.19970.843	weak signal
118.18141.731	binary
118.18797.1397	asymmetry in blue peak
158.27444.129	—
180.22240.202	post-peak blue points preferentially low
401.48229.760	binary
401.48408.649	binary
402.47742.3318	—
402.47799.1736	coherent steep variation in blue
402.47862.1576	binary
402.48280.502	binary
403.47610.576	possible red blend

TABLE 6
EVENT PARAMETERS FROM BLEND FITS

field.tile.seq	$\hat{t}$	$u_{\rm min}$	f_{r_M}	f_{b_M}
101.21689.315	196.6 ± 4.1	0.1609 ± 0.0051	0.726 ± 0.026	0.736 ± 0.026
102.22466.140	148.0 ± 6.9	0.276 ± 0.019	1.059 ± 0.089	1.049 ± 0.088
104.19992.858	103 ± 19	0.52 ± 0.17	1.09 ± 0.56	1.11 ± 0.57
104.20119.6312	46 ± 11	0.56 ± 0.22	0.65 ± 0.40	0.58 ± 0.37
104.20251.1117	68.7 ± 8.0	0.274 ± 0.048	0.413 ± 0.089	0.413 ± 0.089
104.20259.572	14.2 ± 1.5	0.77 ± 0.11	1.01 ± 0.28	1.010 ± 0.27
104.20515.498	43 ± 10	0.92 ± 0.33	1.8 ± 1.3	1.9 ± 1.4
104.20640.8423	78 ± 14	0.178 ± 0.045	0.150 ± 0.043	0.134 ± 0.038
104.20645.3129	133 ± 13	0.78 ± 0.13	1.47 ± 0.44	1.48 ± 0.44
105.21813.2516	17.84 ± 0.72	0.0741 ± 0.0049	0.952 ± 0.062	1.01 ± 0.066
108.18947.3618	46.2 ± 4.2	0.529 ± 0.080	0.95 ± 0.22	1.01 ± 0.23
108.18951.1221	31 ± 22	0.92 ± 0.98	2.7 ± 5.8	2.9 ± 6.2
108.18952.941	63.3 ± 4.3	0.491 ± 0.053	1.14 ± 0.18	1.14 ± 0.18
108.19074.550	12.7 ± 2.0	0.36 ± 0.10	0.44 ± 0.16	0.42 ± 0.15
108.19334.1583	16.7 ± 2.5	0.294 ± 0.067	1.22 ± 0.34	1.19 ± 0.33
109.20119.1051	3.92 ± 0.30	8.75 ± 0.64	1930 ± 550	1840 ± 520
109.20640.360	25.7 ± 9.6	0.84 ± 0.49	$--$	1.4 ± 1.5
110.22455.842	16.5 ± 3.4	0.55 ± 0.17	1.49 ± 0.71	1.50 ± 0.72
113.18552.581	614800 ± 102700	$(1.23 \pm 0.20) \times 10^{-5}$	$(1.03 \pm 0.17) \times 10^{-5}$	$(9.00 \pm 1.50) \times 10^{-6}$
113.18804.1061	19 ± 14	0.17 ± 0.16	0.13 ± 0.14	0.14 ± 0.15
113.19192.365	30 ± 18	0.86 ± 0.84	1.5 ± 2.9	2.0 ± 3.7
114.19712.813	24.0 ± 2.0	0.283 ± 0.036	0.98 ± 0.16	0.97 ± 0.16
114.19846.777	122 ± 14	0.284 ± 0.052	0.226 ± 0.051	0.211 ± 0.048
114.19970.843	16.8 ± 1.5	0.181 ± 0.025	0.79 ± 0.12	0.73 ± 0.11
118.18014.320	15.7 ± 8.6	1.6 ± 1.3	5 ± 11	5 ± 11
118.18271.738	93 ± 17	0.213 ± 0.057	0.35 ± 0.11	0.33 ± 0.10
118.18402.495	26 ± 1.8	0.246 ± 0.027	0.83 ± 0.11	0.85 ± 0.11
118.18797.1397	121.3 ± 2.5	0.1274 ± 0.0039	1.069 ± 0.034	1.043 ± 0.034
118.19182.891	12.48 ± 0.91	0.195 ± 0.030	1.21 ± 0.19	1.22 ± 0.20
118.19184.939	88.5 ± 5.4	0.388 ± 0.037	0.673 ± 0.087	0.675 ± 0.088
121.22032.133	15.0 ± 9.3	1.2 ± 1.2	2.3 ± 5.0	2.4 ± 5.2
158.27444.129	48.7 ± 3.0	0.362 ± 0.036	0.710 ± 0.093	0.689 ± 0.090
162.25865.442	61 ± 10	0.75 ± 0.21	1.01 ± 0.50	0.95 ± 0.47
162.25868.405	30.6 ± 2.5	0.386 ± 0.057	1.00 ± 0.19	1.04 ± 0.20
176.18826.909	3.68 ± 0.38	7.27 ± 0.70	$--$	1120 ± 410
178.23531.931	13.1 ± 2.9	0.54 ± 0.22	1.14 ± 0.71	1.11 ± 0.70
180.22240.202	454 ± 20	0.183 ± 0.010	0.547 ± 0.035	0.551 ± 0.035
401.47991.1840	38 ± 18	0.77 ± 0.62	1.6 ± 2.3	1.6 ± 2.4
401.47994.1182	61 ± 12	0.273 ± 0.085	$--$	0.97 ± 0.36
401.48052.861	83 ± 15	0.304 ± 0.091	0.74 ± 0.28	0.70 ± 0.27
401.48167.1934	48.5 ± 8.2	2.83 ± 0.62	37.1 ± 24.0	39.8 ± 26.0
401.48469.789	7.5 ± 4.2	< 0.26	0.58 ± 0.58	0.54 ± 0.55
402.47678.1666	13.4 ± 6.8	0.45 ± 0.43	1.0 ± 1.4	1.1 ± 1.5
402.47737.1590	11.0 ± 3.5	0.111 ± 0.055	0.26 ± 0.13	0.29 ± 0.15
402.47742.3318	64.7 ± 8.5	0.065 ± 0.020	0.72 ± 0.14	0.61 ± 0.12

TABLE 6—*Continued*

field.tile.seq	$\hat{t}$	$u_{\min}$	f_{r_M}	f_{b_M}
402.47796.1893	21.8 ± 1.4	< 0.03	0.801 ± 0.081	0.832 ± 0.078
402.47798.1259	97800 ± 19500	$(6 \pm 20219) \times 10^{-7}$	$(2.59 \pm 0.52) \times 10^{-4}$	$(2.31 \pm 0.47 \times 10^{-4}$
402.47799.1736	80 ± 44	0.84 ± 0.70	2.5 ± 4.0	2.7 ± 4.4
402.47856.561	52000 ± 16000	$(2.0 \pm 1.1) \times 10^{-5}$	$(3.8 \pm 1.2) \times 10^{-5}$	$(5.0 \pm 1.6) \times 10^{-5}$
402.48158.1296	20.7 ± 4.9	0.148 ± 0.082	0.56 ± 0.26	0.61 ± 0.28
403.47491.770	45.3 ± 5.3	0.494 ± 0.098	1.19 ± 0.35	1.18 ± 0.35
403.47550.807	10.9 ± 1.9	0.33 ± 0.12	1.17 ± 0.47	1.13 ± 0.45
403.47610.576	14.5 ± 1.2	0.123 ± 0.014	0.492 ± 0.059	0.608 ± 0.073
403.47845.495	13.9 ± 2.7	0.62 ± 0.19	1.23 ± 0.64	1.20 ± 0.62

NOTE.—Known binaries and two strong parallax events (104.20251.50 and 104.20382.803) are not included.

TABLE 7

KNOWN BLEND FRACTIONS FOR CLUMP EVENTS WITH BINARY LENSES

Event	f_{r_M}	f_{b_M}
108.18951.593 (97-BLG-28)	1.00	0.90
118.18141.731 (94-BLG-4)	1.06	1.04
401.48408.649 (98-BLG-14)	1.08	1.10

NOTE.—Blend fractions are taken from Alcock et al. (2000c). The errors in blend fractions are $\lesssim 0.05$.

TABLE 8

DATA ON THE 94 BULGE FIELDS.

Field	l	b	$N_{\rm clumps}/100$	$N_{\rm exposures}$	$\epsilon(50{\rm days})$	$\epsilon(200{\rm days})$
101	3.73	−3.02	629.5	804	0.41	0.61
102	3.77	−4.11	444	421	0.24	0.46
103	4.31	−4.62	368	331	0.22	0.37
104	3.11	−3.01	652	1639	0.40	0.59
105	3.23	−3.61	539	640	0.39	0.52
106	3.59	−4.78	346	12	< 0.003	< 0.003
107	4.00	−5.31	269	51	0.007	< 0.003
108	2.30	−2.65	790	1031	0.46	0.74
109	2.45	−3.20	661	761	0.36	0.59
110	2.81	−4.48	408	650	0.33	0.55
111	2.99	−5.14	298	305	0.23	0.37
112	3.40	−5.53	246.5	43	0.005	< 0.003
113	1.63	−2.78	834	1127	0.49	0.73
114	1.81	−3.50	617	776	0.37	0.59
115	2.04	−4.85	325.5	357	0.24	0.35
116	2.38	−5.44	268.5	314	0.21	0.38
117	2.83	−6.00	198	39	0.006	< 0.003
118	0.83	−3.07	741.5	1053	0.44	0.74
119	1.07	−3.83	542.5	1815	0.45	0.68
120	1.64	−4.42	394	676	0.35	0.54
121	1.20	−4.94	344	352	0.22	0.37
122	1.57	−5.45	266	186	0.15	0.23
123	1.95	−6.05	210.5	40	0.006	< 0.003
124	0.57	−5.28	265.5	337	0.22	0.39
125	1.11	−5.93	189	287	0.21	0.37
126	1.35	−6.40	182	36	< 0.003	< 0.003
127	0.28	−5.91	192	178	0.13	0.24
128	2.43	−4.03	516.5	711	0.35	0.55
129	4.58	−5.93	234.5	31	0.006	< 0.003
130	5.11	−6.49	169.5	20	0.02	0.02
131	4.98	−7.33	130	106	0.12	0.22
132	5.44	−7.91	102	180	0.17	0.33
133	6.05	−8.40	70.5	176	0.15	0.18
134	6.34	−9.07	46.5	197	0.09	0.15
135	3.89	−6.26	179	30	0.004	< 0.003
136	4.42	−6.82	137.5	207	0.17	0.26
137	4.31	−7.60	101	193	0.15	0.36
138	4.69	−8.20	95.5	201	0.16	0.21
139	5.35	−8.65	81	191	0.11	0.11
140	5.71	−9.20	64	209	0.13	0.25
141	3.26	−6.59	159	28	0.03	0.03
142	3.81	−7.08	126.5	218	0.15	0.36
143	3.80	−8.00	97	210	0.17	0.25
144	4.68	−9.02	50.5	210	0.10	0.18
145	5.20	−9.50	49.5	210	0.12	0.23
146	3.26	−7.54	106	207	0.19	0.33
147	3.96	−8.81	66	208	0.19	0.20
148	2.33	−6.71	161.5	229	0.18	0.30
149	2.43	−7.43	112.5	236	0.19	0.34

TABLE 8—*Continued*

Field	l	b	$N_{\rm clumps}/100$	$N_{\rm exposures}$	$\epsilon(50{\rm days})$	$\epsilon(200{\rm days})$
150	2.96	−8.01	98.5	229	0.18	0.28
151	3.17	−8.89	85	194	0.14	0.23
152	1.76	−7.07	124	235	0.24	0.32
153	2.11	−7.87	85.5	231	0.17	0.35
154	2.16	−8.51	82	247	0.19	0.20
155	1.01	−7.44	95.5	247	0.17	0.36
156	1.34	−8.12	88.5	249	0.14	0.33
157	0.08	−7.76	105.5	258	0.20	0.37
158	7.08	−4.44	246.5	260	0.20	0.29
159	6.35	−4.40	258.5	464	0.27	0.47
160	6.84	−5.04	248	208	0.15	0.26
161	5.56	−4.01	366	467	0.32	0.45
162	5.64	−4.62	301	382	0.22	0.38
163	5.98	−5.22	259	251	0.19	0.36
164	6.51	−5.90	167.5	20	0.002	< 0.003
165	7.01	−6.38	135	14	< 0.003	< 0.003
166	7.10	−7.07	131.5	110	0.09	0.14
167	4.88	−4.21	388.5	364	0.26	0.40
168	5.01	−4.92	298	210	0.17	0.26
169	5.40	−5.63	208	24	0.004	< 0.003
170	5.81	−6.20	170	17	< 0.003	< 0.003
171	6.42	−6.65	120.5	125	0.15	0.19
172	6.82	−7.61	89	132	0.13	0.18
173	6.92	−8.41	87	146	0.06	0.09
174	5.71	−6.92	143.5	144	0.18	0.22
175	6.10	−7.55	111.5	97	0.06	0.10
176	2.93	−2.30	814.5	423	0.25	0.43
177	6.75	−3.82	319	416	0.30	0.43
178	5.24	−3.42	477	376	0.27	0.41
179	4.92	−2.83	510	349	0.20	0.39
180	5.93	−2.69	478	343	0.21	0.38
301	18.77	−2.05	-	925	0.31	0.46
302	18.09	−2.24	-	365	0.28	0.37
303	17.30	−2.33	-	369	0.23	0.41
304	9.07	−2.70	-	458	0.30	0.50
305	9.69	−2.36	-	411	0.29	0.46
306	8.46	−3.03	-	423	0.28	0.41
307	7.84	−3.37	-	435	0.27	0.43
308	10.02	−2.98	-	360	0.26	0.40
309	9.40	−3.31	-	347	0.23	0.40
310	8.79	−3.64	-	387	0.26	0.43
311	8.17	−3.97	-	396	0.28	0.40
401	2.02	−1.93	964.5	429	0.25	0.45
402	1.27	−2.09	1153	1256	0.26	0.45
403	0.55	−2.32	1085	473	0.26	0.45

NOTE.—Efficiencies (columns 6 and 7) are averaged over $A_{\rm max}$.

TABLE 9
OPTICAL DEPTH BY FIELD

Field	(l, b)	$N_{\rm stars}/100$	$N_{\rm clumps}/100$	$N_{\rm events}$	$\tau/10^{-6}$
101	$(3.73, -3.02)$	6284	629.5	1	1.62 ± 1.62
102	$(3.77, -4.11)$	6545	444	1	3.67 ± 3.67
104	$(3.11, -3.01)$	5813	652	9	8.76 ± 3.73
105	$(3.23, -3.61)$	6375	539	1	0.35 ± 0.35
108*	$(2.30, -2.65)$	6498	790	6	2.04 ± 0.92
109*	$(2.45, -3.20)$	6926	661	2	0.58 ± 0.41
110	$(2.81, -4.48)$	6649	408	1	0.46 ± 0.46
113*	$(1.63, -2.78)$	6252	834	3	0.55 ± 0.35
114*	$(1.81, -3.50)$	6665	617	3	1.19 ± 0.74
118*	$(0.83, -3.07)$	6347	741.5	7	2.85 ± 1.35
119*	$(1.07, -3.83)$	7454	542.5	0	—
121	$(1.20, -4.94)$	5855	344	1	0.59 ± 0.59
158	$(7.08, -4.44)$	4703	246.5	1	2.96 ± 2.96
162	$(5.64, -4.62)$	5914	301	2	3.11 ± 2.21
176	$(2.93, -2.30)$	7741	814.5	1	0.37 ± 0.37
178	$(5.24, -3.42)$	8186	477	1	0.43 ± 0.43
180	$(5.93, -2.69)$	6388	478	1	4.62 ± 4.62
401*	$(2.02, -1.92)$	6630	964.5	7	5.13 ± 2.16
402*	$(1.27, -2.09)$	7098	1153	10	3.95 ± 1.50
403*	$(0.55, -2.32)$	6798	1085	4	1.16 ± 0.66
CGR[a]	$(1.50, -2.68)$	60668	7388.5	42	$2.17^{+0.47}_{-0.38}$

NOTE.—Only fields with at least one clump giant event (and field 119) are shown.

*Field is near the Galactic center and included in CGR.

[a]Average towards the group of 9 fields designated as CGR.

TABLE 10

ONE SIGMA UPPER LIMITS ON THE OPTICAL DEPTH FOR FIELDS WITH NO CLUMP EVENTS

field	$\tau^{\rm lim,1\sigma}$	Field	$\tau^{\rm lim,1\sigma}$	Field	$\tau^{\rm lim,1\sigma}$	Field	$\tau^{\rm lim,1\sigma}$
103	3.26×10^{-6}	128	1.45×10^{-6}	144	4.62×10^{-5}	161	2.52×10^{-6}
106	7.90×10^{-6}	129	9.87×10^{-5}	145	4.10×10^{-5}	163	5.84×10^{-6}
107	4.22×10^{-5}	130	1.13×10^{-4}	146	1.42×10^{-5}	164	3.68×10^{-4}
111	4.56×10^{-6}	131	2.01×10^{-5}	147	3.10×10^{-5}	165	6.81×10^{-4}
112	7.12×10^{-5}	132	2.04×10^{-5}	148	9.71×10^{-6}	166	2.52×10^{-5}
115	3.58×10^{-6}	133	3.25×10^{-5}	149	1.39×10^{-5}	167	2.83×10^{-6}
116	5.02×10^{-6}	134	5.45×10^{-5}	150	1.59×10^{-5}	168	6.30×10^{-6}
117	8.37×10^{-5}	135	9.14×10^{-5}	151	2.67×10^{-5}	169	1.05×10^{-4}
119	1.10×10^{-6}	136	1.23×10^{-5}	152	1.18×10^{-5}	170	4.54×10^{-4}
120	1.91×10^{-6}	137	1.72×10^{-5}	153	1.83×10^{-5}	171	2.08×10^{-5}
122	6.90×10^{-6}	138	1.97×10^{-5}	154	2.14×10^{-5}	172	2.91×10^{-5}
123	7.70×10^{-5}	139	2.80×10^{-5}	155	1.65×10^{-5}	173	4.44×10^{-5}
124	4.94×10^{-6}	140	3.42×10^{-5}	156	1.85×10^{-5}	174	1.36×10^{-5}
125	7.95×10^{-6}	141	9.01×10^{-5}	157	1.39×10^{-5}	175	3.58×10^{-5}
126	1.35×10^{-4}	142	1.28×10^{-5}	159	3.57×10^{-6}	177	3.09×10^{-6}
127	1.02×10^{-5}	143	1.80×10^{-5}	160	8.12×10^{-6}	179	2.61×10^{-6}

TABLE 11

EVENTS FROM THE SAMPLE MADE ROBUST AGAINST BLENDING

Event	$\delta_{\rm blue}$	Event	$\delta_{\rm blue}$
108.18947.3618	0.04	102.22466.140	0.55
108.18951.1221	0.31	104.19992.858	0.20
108.18952.941	0.74	104.20119.6312	−1.14
108.19334.1583	0.56	104.20259.572	0.02
109.20640.360	0.25	104.20515.498	0.66
113.19192.365	0.27	104.20645.3129	1.08
114.19712.813	−0.20	105.21813.2516	0.15
118.18014.320	0.40	110.22455.842	0.70
118.18402.495	−1.35	121.22032.133	0.26
118.18797.1397	1.28	162.25865.442	−0.12
118.19182.891	1.11	162.25868.405	0.21
401.47991.1840	0.27	178.23531.931	0.16
401.47994.1182	−0.08		
401.48052.861	−1.13		
401.48167.1934	1.49		
401.48469.789	−0.83		
402.47678.1666	0.07		
402.47799.1736	0.40		
402.48158.1296	−1.39		
403.47491.770	0.51		
403.47550.807	0.28		
403.47845.495	0.32		

NOTE.—Events in CGR are displayed in the left column and events in the remaining fields in the right column.

TABLE 12
OPTICAL DEPTH BY FIELD FROM VERIFICATION SAMPLE

Field	$N_{\rm events}^{\rm ver}$	$\tau^{\rm ver}/10^{-6}$	$N_{\rm events}^{\rm orig}$	$\tau/10^{-6}$
108	4	2.25 ± 1.20	6	2.04 ± 0.92
109	1	0.59 ± 0.59	2	0.58 ± 0.41
113	1	0.80 ± 0.80	3	0.55 ± 0.35
114	1	1.07 ± 1.07	3	1.19 ± 0.74
118	4	2.77 ± 1.85	7	2.85 ± 1.34
119	0	—	0	—
401	5	5.41 ± 2.67	7	5.13 ± 2.16
402	3	4.55 ± 3.42	10	3.95 ± 1.50
403	3	1.29 ± 0.85	4	1.16 ± 0.66
101	0	—	1	1.62 ± 1.62
102	1	3.67 ± 3.67	1	3.67 ± 3.67
104	5	6.07 ± 3.18	9	8.76 ± 3.73
105	1	0.35 ± 0.35	1	0.35 ± 0.35
110	1	0.46 ± 0.46	1	0.46 ± 0.46
121	1	0.59 ± 0.59	1	0.59 ± 0.59
158	0	—	1	2.96 ± 2.96
162	2	3.11 ± 2.21	2	3.11 ± 2.21
176	0	—	1	0.37 ± 0.37
178	1	0.43 ± 0.43	1	0.43 ± 0.43
180	0	—	1	4.62 ± 4.62